Nuclear Quantum Effects in Gas-Phase 2-Fluoroethanol

Mrinal Arandhara and Sai G. Ramesh[a]

Dept. of Inorganic and Physical Chemistry, Indian Institute of Science,
Bangalore 560012, India

Torsional motions along the FCCO and HOCC dihedrals lead to the five unique conformations of 2-fluoroethanol, of which the gauche conformer along both dihedrals has the lowest energy. In this work, we explore how nuclear quantum effects (NQEs) are manifest in the structural parameters of the lowest energy conformer, in the intramolecular free energy landscape along the FCCO and HOCC dihedrals, and also in the infrared spectrum of the title molecule, through the use of path integral simulations. We have first developed a full dimensional potential energy surface using the reaction surface Hamiltonian framework. On this potential, we have carried out path integral molecular dynamics simulations at several temperatures starting from the minimum energy well to explore structural influences of NQEs including geometrical markers of the interaction between the OH and F groups. From the computed free energy landscapes, significant reduction of the torsional barrier is found at low temperature near the cis region of the dihedrals, which can be understood through the trends in the radii of gyration of the atomic ring polymers. We find that the inclusion of NQEs in the computation of infrared spectrum is important to obtain good agreement with the experimental band positions.

---

[a] Corresponding author. Emails: (MA) mrinala@iisc.ac.in; (SGR) sairamesh@iisc.ac.in

I. INTRODUCTION

A quantum description of nuclear motion is important for a complete description of molecular vibrations. Typical approaches towards this include the eigensolutions of the rovibrational Hamiltonian for spectroscopy or wavepacket simulations for chemical dynamics. However, such routes are computationally impeded due to the high dimensionality to be addressed even for medium-sized molecules, despite modern hardware. A well-known alternative approach is based on the path integral formalism,[1] where the classical isomorphism between a quantum particle and a chain of classical particles is employed.[2] This allows the use of molecular simulation techniques to address nuclear quantum effects (NQEs), and has enjoyed much success in the recent years.[3] Path integral molecular dynamics (PIMD),[4–6] centroid molecular dynamics (CMD),[7–9] and ring polymer molecular dynamics (RPMD)[10–12] methods and their variants have been applied to wide variety of systems.[13–27]

The present work explores the NQEs in 2-fluoroethanol (2FE). As part of the set of 2-X-ethanols (X=F, OH, NH_2), 2FE has been well-explored from both experiments and theory with regards to its various conformations – preference of the gauche form, whether there is an intramolecular O-H$\cdots$F H-bond and strength of intramolecular interactions – and vibrational spectroscopy.[28–36] These studies have pointed to insufficient experimental and theoretical evidence in favour of intramolecular H-bonding. However, Rosenberg[36] has suggested in recent work on 2-X-ethanols on the basis of analyses of non-covalent interactions and contrast of inter versus intramolecular H-bonding energetics and geometrical parameters that, albeit weak, they may be termed as intramolecular H-bonds. In particular, as the XCCO torsion goes towards 0°, an enhancement of the O-H and X interaction is observed, including the appearance of a bond critical point from QTAIM analysis below a certain angle.

Theoretical studies on 2FE conducted so far have been computations of various stationary points, their relative energies and relaxed potential energy landscapes along the FCCO torsion.[31,32,35,36] An aim of the present study is to analyse how the NQEs affect the O-H and F interaction. Consequent to zero-points energy effects and competing influences that determine its magnitude, shortening of the donor-acceptor distances and elongation of the OH bond occur for typical strength H-bonds.[16,37–39] Despite the relatively weak OH and F intramolecular interaction in 2FE, we wish to understand how nuclear quantization affects the distances and angles between the OH and F groups.

Another aspect of interest is the modulation of the conformational landscape of 2FE due to NQEs. While relaxed ab initio and classical free energy profiles along its large amplitude motions may be similar, the inclusion of ZPE effects may further modify the relative energies of the minima as well as barriers, and thereby affect dynamics. For 2FE, conformational isomerization upon CH or OH excitation and the intramolecular vibrational energy redistribution that drives it have been studied previously via experiments.[40–44] The work of Durig et al. provides an effective one-dimensional FCCO torsional model potential, fitted through torsional transitions of 2FE.[34] However, to the best of our knowledge, there has been no direct theoretical exploration of the free energy landscape in the space of the FCCO and HOCC dihedrals so far for this model molecule. The second aim of this work is to compute and contrast such landscapes from classical and path integral quantum simulations.

It is worth mentioning that path integral treatments on systems with large amplitude motions, including torsional modes and reaction coordinates, have been of recent interest. For example, the study of the three torsions of glycine by Miller and Clary[45] showed that conformer populations are significantly affected by NQEs compared to a classical treatment. Drechsel-Grau and Marx found that the barrier for collective proton tunneling in hexagonal ice crystals is somewhat reduced by NQEs at 300 K compared to classical simulations, but very strongly lowered at 50 K where the system enters a deep tunneling regime with an effective barrier of about a fifth of the classical one.[20] Earlier work of Markland et al. found similar low temperature tunneling behaviour in the diffusion of H and Mu atoms along the c-axis of hexagonal ice.[46] Access to a similar quantum regime was also found in recent work by Mendez et al. for the exchange of dangling and H-bonded hydrogens (bifurcation pathway) in H_2O-H_2O, H_2O-CH_3OH and H_2O-NH_3 dimers in the 20-50 K range, where they additionally explored isotope effects.[23,25] Videla et al. showed the reduction of such exchange barriers at 75 K for both $(H_2O)_3$ and $(D_2O)_3$ compared to classical simulations.[21] Bajaj et al. explored similar quantum effects for the $I^-{\cdot}(H_2O)_2$ and its perdeuterated analogue and also found a systematic lowering of barriers along the bifurcation pathway.[22] Sauceda et al. showed how delocalization of the methyl hydrogens in toluene upon quantum treatment leads to an effective higher barrier for the torsional motion.[26] The study of the free energy landscape of 2FE draws inspiration from such studies. As noted further above, prior ab initio calculations have shown evidence for strengthening of the OH and F interaction as the FCCO torsional angle is reduced.[36] This suggests the possibility that attendant quantum effects may further favour the interaction and lower the direct barrier between enantiomeric forms of 2FE. A comparison of classical and quantum (path integral) free energy landscapes would reveal the extent of such effects. In a future work, ethylene glycol will be similarly explored;[47] the work of Rosenberg predicted a favourable interaction at lower values of the OCCO dihedral in this molecule as well.

A fruitful treatment of NQEs requires a high-quality potential energy surface (PES) on which the simulations are carried out. One approach is the use of on-the-fly ab initio calculations to compute the energies and forces directly. Of course, this becomes quickly expensive for systems beyond a few atoms and as the number of ring polymer beads in the path integral simulations increase (e.g. at very low temperatures). The development of a high-quality model PES allows for both longer simulations and the use of more beads to converge the quantum effects. Noting that a full-dimensional PES for 2FE is not yet available in the literature, we have built one in this work, along with a dipole moment surface (DMS). We have computed the infrared spectrum of 2FE from classical and path integral simulations. This would provide a direct analysis of the role and importance of quantum effects in a measurable property, which constitutes the third aim of this work. The experimental spectral band centres from the study by Durig et al. provide the data for comparison.[34]

This paper is organized as follows. Section II discusses the various stationary points of 2FE and the modelling of a full-dimensional PES based on a reaction surface Hamiltonian approach as well as a dipole moment surface along similar lines. Details of quantum mechanical simulations carried out on it, viz. path integral molecular dynamics (PIMD), path-integral well-tempered metadynamics (PI-WTmetaD) along the FCCO and CCOH dihedrals, umbrella sampling simulations along the FCCO dihedral, and the computation of infrared spectrum with thermostatted ring polymer molecular dynamics (T-RPMD) are

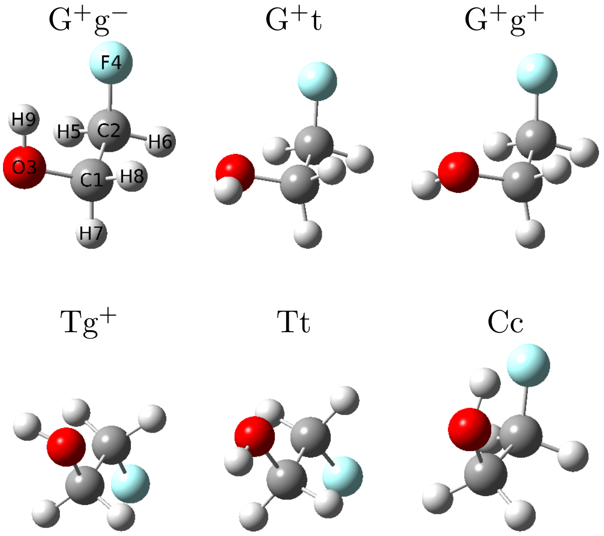

FIG. 1. Stationary points of 2FE. The geometries are optimized at the MP2/aVTZ level of theory. The G^+g^- structure and its equivalent form G^-g^+ (not shown, obtained by the transformation $(\phi_1, \phi_2) \rightarrow (-\phi_1, -\phi_2)$) are the minimum energy conformers. Other gauche and trans conformers and their equivalent forms are higher energy minima, while Cc is a saddle point. The uppercase/lowercase notation refer to the FCCO/HOCC torsions. The relative energies and geometrical parameters of the structures is given in Table I.

given. Section III begins with the quality of the PES and DMS developed, followed by results from the PIMD, WT-metaD, umbrella sampling and infrared spectrum calculations along with the discussion of the observed quantum effects. Section IV provides a brief summary.

II. METHODOLOGY

A. Stationary points

Fig. 1 shows the key stationary points of 2FE. There are nine minima, arising from combinations of gauche and trans conformations of the FCCO (ϕ_1) and and HOCC (ϕ_2) dihedrals. Four pairs are symmetrically equivalent through the transformation $(\phi_1, \phi_2) \rightarrow (-\phi_1, -\phi_2)$; one member of each pair is depicted in Fig. 1. The global minima are the equivalent gauche structures G^+g^- and G^-g^+. The upper- and lowercase notation refers to the FCCO and HOCC dihedrals, respectively. The minima and all other optimized structures in this work have been obtained at the MP2 level of theory with the aug-cc-pVTZ (aVTZ) basis using the Gaussian 16 package.[48] The relative energies of all minima are given in Table I along with their internal coordinates. Relative energies of the minima at other method/basis combinations is provided in Table S-1 (Supplementary Material). Also given in both tables are the energy and structure of the Cc transition state (TS) that lies between the two global minima and is the highest energy saddle point in the (ϕ_1, ϕ_2) space. The MP2/aVTZ normal mode frequencies for all structures are given in Table S-2.

TABLE I. Energies and geometries of stationary points of 2FE at the MP2/aVTZ level of theory. The energies (in cm^{-1}) are relative to the global minimum structures, G^+g^- and G^-g^+. All bond lengths are in Å while all angles and dihedrals are in degrees. Equivalent structures that have the same energy are obtained by the transformation $(\phi_1, \phi_2) \rightarrow (-\phi_1, -\phi_2)$ and attendant changes in internals, some of which remain the same , and others are exchanged; see text.

		G^+g^-	G^+t	Tt	Tg^+	G^+g^+	Cc
ϕ_1	$\phi(F_4C_2C_1O_3)$	63.6	72.2	180.0	178.9	65.2	0.0
ϕ_2	$\phi(H_9O_3C_1C_2)$	−58.0	−167.2	180.0	76.1	63.2	0.0
E		0.0	685.6	755.6	813.6	861.0	2386.8
R_1	$r(C_2C_1)$	1.5045	1.5019	1.5105	1.5145	1.5071	1.5454
R_2	$r(O_3C_1)$	1.4181	1.4209	1.4233	1.4226	1.4181	1.4161
R_3	$r(F_4C_2)$	1.3991	1.3901	1.3916	1.3922	1.3880	1.3986
R_4	$r(H_5C_2)$	1.0888	1.0894	1.0885	1.0885	1.0919	1.0870
R_5	$r(H_6C_2)$	1.0898	1.0901	1.0885	1.0908	1.0912	1.0870
R_6	$r(H_7C_1)$	1.0895	1.0951	1.0921	1.0918	1.0956	1.0905
R_7	$r(H_8C_1)$	1.0936	1.0925	1.0921	1.0876	1.0883	1.0905
R_8	$r(H_9O_3)$	0.9640	0.9616	0.9615	0.9623	0.9628	0.9642
R_9	$\theta(O_3C_1C_2)$	111.8	108.2	105.6	110.3	113.6	112.9
R_{10}	$\theta(F_4C_2C_1)$	108.5	110.4	108.6	109.1	110.6	110.0
R_{11}	$\theta(H_5C_2C_1)$	111.1	110.3	110.8	110.7	111.2	111.7
R_{12}	$\theta(H_6C_2C_1)$	111.4	110.3	110.8	111.1	110.1	111.7
R_{13}	$\theta(H_7C_1C_2)$	109.2	108.2	109.5	109.9	108.2	109.3
R_{14}	$\theta(H_8C_1C_2)$	109.4	109.0	109.5	109.7	109.3	109.3
R_{15}	$\theta(H_9O_3C_1)$	107.0	108.6	108.4	108.3	108.4	107.3
R_{16}	$\phi(H_5C_2C_1F_4)$	−117.8	−119.1	−119.0	−119.3	−119.4	−118.3
R_{17}	$\phi(H_6C_2C_1F_4)$	118.6	119.0	119.0	118.9	119.3	118.3
R_{18}	$\phi(H_7C_1C_2O_3)$	117.8	120.5	120.4	124.0	124.5	121.0
R_{19}	$\phi(H_8C_1C_2O_3)$	−123.7	−121.4	−120.4	−117.1	−117.9	−121.0
Equiv. struct.		G^-g^+	G^-t		Tg^-	G^-g^-	

Figure 2 shows the relaxed potential energy surface as a function of the (ϕ_1, ϕ_2). The plot indicates lower barriers for the ϕ_2 torsion compared to those for ϕ_1, which points to the relative ease of rotation of the OH group about the CO bond. The plot also suggests that the $G^+ \leftrightarrow T \leftrightarrow G^-$ is more feasible than direct interconversion through Cc. One of the goals of this work is to explore how NQEs modify this landscape. To this end, we begin with the development of a full-dimensional model potential energy surface for 2FE.

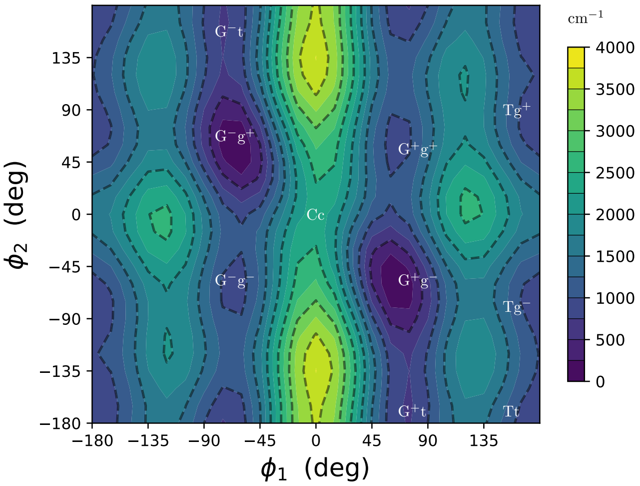

FIG. 2. Relaxed ab initio MP2/aVTZ potential surface for 2FE as a function of the FCCO (ϕ_1) and HOCC (ϕ_2) dihedrals. Both angles were sampled at 15° intervals.

B. PES modelling

Drawing from the reaction surface Hamiltonian approach,[49–52] we write the potential expansion for 2FE as

$$V(\boldsymbol{S}, \phi_1, \phi_2) = V_{rs}(\phi_1, \phi_2) + V_b(\boldsymbol{S}|\phi_1, \phi_2). \tag{1}$$

V_{rs} is the dihedral potential surface obtained by relaxing all other internals, while V_b accounts for displacements along these internals from the relaxed geometries. The optimization leading to V_{rs} is carried out at the MP2/aVTZ level of theory. The energies so obtained are used to model V_{rs} as a double Fourier expansion:[53]

$$\begin{aligned} V_{rs}(\phi_1, \phi_2) = &\sum_{m=0}^{M_{max}} \sum_{n=0}^{N_{max}} A^{(1)}_{mn} \cos(m\phi_1)\cos(n\phi_2) \\ &+ \sum_{m=1}^{M_{max}} \sum_{n=1}^{N_{max}} A^{(2)}_{mn} \sin(m\phi_1)\sin(n\phi_2). \end{aligned} \tag{2}$$

The form satisfies the required symmetry relation $V_{rs}(\phi_1, \phi_2) = V_{rs}(-\phi_1, -\phi_2)$. The coefficients of the expansion are determined by generalized linear least squares fitting with a sufficient number of unique sample ab initio data points in (ϕ_1, ϕ_2) space, including those listed in Table I.

Before discussing the rest of the potential expansion, we dwell on the symmetry of physical quantities of 2FE. This is ascertained by the effect of the transformation $\hat{\pi} : \ (\phi_1, \phi_2) \rightarrow (-\phi_1, -\phi_2)$. Quantities are denoted even/odd if they retain/change sign upon the action of $\hat{\pi}$:

$$\begin{aligned} \hat{\pi} Y_e(\phi_1, \phi_2) = Y_e(-\phi_1, -\phi_2) &= \ \ \, Y_e(\phi_1, \phi_2), \\ \hat{\pi} Y_o(\phi_1, \phi_2) = Y_o(-\phi_1, -\phi_2) &= -Y_o(\phi_1, \phi_2). \end{aligned} \tag{3}$$

TABLE II. Definition of symmetrized internals on 2FE and their symmetry with respect to the operation $\hat{\pi} : (\phi_1, \phi_2) \rightarrow (-\phi_1, -\phi_2)$.

Coord.	Definition	Sym
S_1	R_1	even
S_2	R_2	even
S_3	R_3	even
S_4	$(R_4 + R_5)/\sqrt{2}$	even
S_5	$(R_4 - R_5)/\sqrt{2}$	odd
S_6	$(R_6 + R_7)/\sqrt{2}$	even
S_7	$(R_6 - R_7)/\sqrt{2}$	odd
S_8	R_8	even
S_9	R_9	even
S_{10}	R_{10}	even
S_{11}	$(R_{11} + R_{12})/\sqrt{2}$	even
S_{12}	$(R_{11} - R_{12})/\sqrt{2}$	odd
S_{13}	$(R_{13} + R_{14})/\sqrt{2}$	even
S_{14}	$(R_{13} - R_{14})/\sqrt{2}$	odd
S_{15}	R_{15}	even
S_{16}	$(R_{16} + R_{17})/\sqrt{2}$	odd
S_{17}	$(R_{16} - R_{17})/\sqrt{2}$	even
S_{18}	$(R_{18} + R_{19})/\sqrt{2}$	odd
S_{19}	$(R_{18} - R_{19})/\sqrt{2}$	even

In accordance with the symmetry, the dihedral expansion for an even quantity is given as

$$\begin{aligned} \underset{(even)}{Y_e(\phi_1, \phi_2)} = & \sum_{m=0}^{M_{max}} \sum_{n=0}^{N_{max}} A^{(1)}_{e;mn} \cos(m\phi_1) \cos(n\phi_2) \\ & + \sum_{m=1}^{M_{max}} \sum_{n=1}^{N_{max}} A^{(2)}_{e;mn} \sin(m\phi_1) \sin(n\phi_2), \end{aligned} \tag{4}$$

while that for an odd quantity is given as

$$\begin{aligned} \underset{(odd)}{Y_o(\phi_1, \phi_2)} = & \sum_{m=0}^{M_{max}} \sum_{n=1}^{N_{max}} A^{(1)}_{o;mn} \cos(m\phi_1) \sin(n\phi_2) \\ & + \sum_{m=1}^{M_{max}} \sum_{n=0}^{N_{max}} A^{(2)}_{o;mn} \sin(m\phi_1) \cos(n\phi_2). \end{aligned} \tag{5}$$

These expansions up to orders (M_{max}, N_{max}) along (ϕ_1, ϕ_2) are extensively used in the present work.

The V_b term in Eq. (1) involves displacements in all other (19) internals. Denoting the bond distances, angles and dihedrals as $\boldsymbol{R}$, their values at the optimal geometries as a function of (ϕ_1, ϕ_2), denoted $\boldsymbol{R}^\circ$, are given in Table I. As for V_{rs}, symmetry dictates that

$V_b(\phi_1, \phi_2) = V_b(-\phi_1, -\phi_2)$. Furthermore, terms involving internals in V_b are required to be even with respect to $\hat{\pi}$. The internal coordinates associated with the C, F, O, and hydroxyl H atoms are even. For instance, it is readily observed that the hydroxyl bond length is invariant to $\hat{\pi}$, i.e. $R_8^\circ(\phi_1, \phi_2) = R_8^\circ(-\phi_1, -\phi_2)$. In contrast, the bond distances, angles and dihedrals belonging to the CH hydrogens are neither even nor odd. This occurs because the values of the internals are exchanged between the H atoms attached to a given C atom. For instance, for C_2H_5 (R_4°) and C_2H_6 (R_5°) optimal bond lengths one finds $R_4^\circ(\phi_1, \phi_2) = R_5^\circ(-\phi_1, -\phi_2)$ and $R_5^\circ(\phi_1, \phi_2) = R_4^\circ(-\phi_1, -\phi_2)$. However, simple linear combinations $S_{4,5} = (R_4 \pm R_5)/\sqrt{2}$ do show even and odd symmetry: $S_4^\circ(\phi_1, \phi_2) = S_4^\circ(-\phi_1, -\phi_2)$ while $S_5^\circ(\phi_1, \phi_2) = -S_5^\circ(-\phi_1, -\phi_2)$. Similar symmetry-adapted coordinates are defined for the other bonds, angles and dihedrals for the CH hydrogens, while the internals of the F, C, O and hydroxyl H are merely relabelled. The full set $\boldsymbol{S}$ of symmetry adapted internals are defined in Table II.

With their symmetry defined, the optimal value of each symmetry-adapted internal on the dihedral surface $S_j^\circ(\phi_1, \phi_2)$ can be expanded to high accuracy using Eq. (4) or (5) as appropriate. These are then used to define displacements $\delta S_j = S_j - S_j^\circ(\phi_1, \phi_2)$ as displacements relative to the dihedral surface. It is convenient to use dimensionless coordinates, $s_j = S_j/\{\hbar^2 G_{jj}/F_{jj}\}^{1/4}$, where G_{jj} and F_{jj} are diagonal elements of Wilson F and G matrices defined at the G^+g^- global minimum.

The V_b term can be expanded in terms of dimensionless displacements as follows:

$$\begin{aligned} V_b(\boldsymbol{S}|\phi_1, \phi_2) = & \sum_{i \le j} f_{ij}^{(2)}(\phi_1, \phi_2)\delta s_i \delta s_j \\ & + \sum_{i \le j \le k} f_{ijk}^{(3)}(\phi_1, \phi_2)\delta s_i \delta s_j \delta s_k \\ & + \sum_{i \le j \le k \le l}{}' f_{ijkl}^{(4)}(\phi_1, \phi_2)\delta s_i \delta s_j \delta s_k \delta s_l \\ & + \sum_{i}{}'' \sum_{n=5}^{8} f_i^{(n)} \delta s_i^n \\ & + \sum_{i,j}{}''' \sum_{n=5}^{8} \sum_{m=0}^{n} f_{ij;m}^{(n)} \delta s_i^{n-m} \delta s_j^m . \end{aligned} \tag{6}$$

Each $f_{ij\ldots}$ term above is in energy (cm^{-1}) units. The primes on the summations indicate index restrictions. The first three terms on the RHS are the quadratic, cubic and quartic expansion terms. The quartic derivatives are restricted to three-body terms. The last two summations of V_b involve one-body high order expansion terms for all bonds and angles only, which were found necessary to include for better accuracy at large displacements. The fourth term is restricted to coordinates S_j that are identical to the parent internals R_j, while the fifth term is restricted to coordinate pairs (S_i, S_j) that are symmetry-adapted ones through linear combinations of (R_i, R_j) pairs; see Table II.

Each term on the RHS involves a product of powers of δs's, which is either even or odd. Correspondingly, the expansion of each force constant term in terms of (ϕ_1, ϕ_2) would be even or odd, so that V_b is even. In order to obtain the expansion, the force constants were first obtained at a sufficient number of points on the dihedral surface. The quadratic force constants were computed by transforming the Hessians in Cartesian form to those in terms of dimensionless symmetrized internals. Cubic and quartic force constants were obtained by five-point numerical differentiation of quadratic ones obtained at S_j displaced from the relaxed dihedral surface, for which step sizes of 0.002 Å for bonds and 0.1° for angles and dihedrals were found to yield stable derivatives.

We note that while the quadratic terms of V_b were obtained at the MP2/aVTZ level, we have used the aug-cc-pVDZ (aVDZ) basis instead to obtain the cubic and higher derivatives of V_b. Given the need to compute derivatives at a few hundred points in the dihedral space and hence a large total number of high order derivatives to be calculated, the larger aVTZ basis was found very expensive. The smaller aVDZ basis strongly reduces the computational time. For the correct evaluation of the third and higher derivatives, the dihedral surface has been reoptimized at the MP2/aVDZ level. In effect, we have developed a full auxilliary potential with the smaller basis and then used its third and higher order terms along with V_{rs}, $\boldsymbol{S}^\circ$ and quadratic terms of V_b at the MP2/aVTZ level. We have also verified from sample calculations at select points that the difference between higher derivatives obtained with the two bases is small compared to the size of the corresponding term. Consequently, an accurate PES is obtained with this approach, as will be shown further below in Section III A.

For the higher order derivatives, ab initio MP2/aVDZ energies at one-mode displaced geometries along each (unsymmetrized) stretch and bend were computed at large displacements. We used $R_j^\circ - 0.3\text{Å} \leq R_j \leq R_j^\circ + 0.45\text{Å}$ with a step size of 0.0375Å for all stretches, $R_j^\circ - 32^\circ \leq R_j \leq R_j^\circ + 40^\circ$ with a step size of 4° for all bends, except the COH bend for which a larger range of $R_j^\circ - 45^\circ \leq R_j \leq R_j^\circ + 50^\circ$ with a step size of 5° was used. The quintic up to octic terms were fitted along each such R_j after subtracting the previously obtained contributions up to quartic order (at the MP2/aVDZ level). The computation of one-mode high order derivatives assumes that high-order coupling terms involving two or more Rs is negligible. Finally, the derivatives were transformed to S_j, leading to the last two terms of V_b.

With various derivatives obtained at a sufficiently large set of points on the dihedral surface, they are fitted to even or odd expansion (see Eqs. (4) and (5)). The (M_{max}, N_{max}) values are chosen by trial and error to be large enough for high accuracy while avoiding overfitting. The full-dimensional potential for 2FE as defined by Eqs. (1) and (6) uses two basis sets, which we denote as the MP2/aVTZ+DZ PES for this molecule. The quality of this PES is discussed in Section III A.

C. DMS modelling

Towards the computation of infrared spectra for 2FE via path integral simulations, we have fitted a dipole moment surface of the form

$$\begin{aligned}\boldsymbol{\mu} &= \boldsymbol{\mu}_{rs} + \boldsymbol{\mu}_b \\ &= \sum_k q_{rs,k}(\phi_1, \phi_2)\boldsymbol{r}_k + \sum_k q_{b,k}(\delta\boldsymbol{S}|\phi_1, \phi_2)\boldsymbol{r}_k.\end{aligned} \tag{7}$$

The above partitioning of $\boldsymbol{\mu}$ into reaction surface and remainder components is carried out in the same manner as done for the potential (Eq. 1). As shown in an earlier work[54] , the dipole moment surface may be modelled through the set of scalar atomic charges ($q_k = q_{rs,k} + q_{b,k}$, where k is the atom number) that are functionally dependent on internal coordinates and atom positions ($\boldsymbol{r}_k$). Presently, we expand the charges in terms of the reaction surface modes (ϕ_1, ϕ_2) and other internals ($\boldsymbol{S}$) in a manner similar to terms in the potential.

The reaction surface atomic charges, $q_{rs,k}(\phi_1, \phi_2)$, are fitted to individual dihedral expansions. The reference values are taken as HLY charges obtained at the same geometries used for the modelling of V_{rs}. However, the charges on the CH hydrogen atoms do not have definite even/odd symmetry, just as their internals R also do not have definite symmetry. As shown in Table II, the difficulty is readily overcome by taking sum and difference combinations. We apply this to the atomic charges as well, which are then readily fitted to even/odd expansions in (ϕ_1, ϕ_2) as per Eqs. (4) and (5). With suitable expansion sizes, accurate fits for $\boldsymbol{\mu}_{rs}$ are obtained.

For the fitting of $\boldsymbol{\mu}_b$, we have limited the expansion of other internals $\boldsymbol{S}$ in $q_{b,k}$ to first order,

$$\begin{aligned} \boldsymbol{\mu}_b(\delta\boldsymbol{S}|\phi_1, \phi_2) &= \sum_k q_{b,k}(\delta\boldsymbol{S}|\phi_1, \phi_2)\boldsymbol{r}_k \\ &= \sum_k \sum_j f_{b,kj}(\phi_1, \phi_2)\delta s_j \boldsymbol{r}_k, \end{aligned} \tag{8}$$

since higher order expansions leads to a strong increase in the number of parameters to be determined. The $f_{b,kj}$ are essentially the derivatives of the first $q_{b,k}$ along various dimensionless internals, s_j. Although we first attempted to use numerical derivatives of HLY charges, these were found to have discontinuities in (ϕ_1, ϕ_2) space. Instead, we have directly fitted the residual dipole function $\boldsymbol{\mu}_b^{ab} = \boldsymbol{\mu} - \boldsymbol{\mu}_{rs}^{ab}$, where the $\boldsymbol{\mu}_{rs}^{ab}$ is the reaction surface dipole function using the ab initio rather than fitted charges, as follows. (1) The residual $\boldsymbol{\mu}_b^{ab}$ is determined at displacements of ±0.03 Å and ±0.04 Å for bonds and ±1.5° and ±2.0° for angles and dihedrals from each of the reaction surface points used for $\boldsymbol{\mu}_{rs}$. (2) The molecular frame is fixed by choosing the CC bond axis as $\hat{x}$ and using the C-C-O plane to define the xy plane. All geometries and hence dipole components are rotated to this frame. (3) Like the $q_{rs,k}$ for the H atoms, the corresponding charges $q_{b,k}$ are neither even nor odd functions of (ϕ_1, ϕ_2). By taking sum and difference combinations of the charges and also Cartesian coordinates of CH hydrogen atoms, the equation is symmetrized. Consequently, the modified $f_{b,kj}$ expansion coefficients are even/odd functions in (ϕ_1, ϕ_2). (4) The expansion coefficients are also constrained by a charge neutrality condition, $\sum_k q_{b,k} = 0$. Note that such a restraint is already present in the HLY charges used to fit the $q_{rs,k}$. Using all the geometries discussed above, a system of linear equations[54] is prepared including the dihedral even/odd expansions as appropriate, and solved using the singular value decomposition (SVD) method from the Numpy package.[55] With appropriate dihedral expansion (M_{max}, N_{max}) sizes, accurate $\boldsymbol{\mu}_b$ fits are obtained.

D. Dynamical simulations

The NQEs in 2FE were studied using simulations techniques based on the path integral approach, viz. PIMD[4–6] and T-RPMD.[10,12,56] With the former method, we have also used the enhanced sampling methods of umbrella sampling[57] and well-tempered metadynamics.[58–61] For all simulations discussed below, home-built codes were used. Interfaces to PLUMED 2.8.0[62] were used for the enhanced sampling methods. The details of each of these simulations are given in the following sections.

1. *PIMD simulations*

We have carried out PIMD simulations for 2FE at 50 K, 100 K, 200 K and 300 K for both 2FE-$h5$ (normal form) and 2FE-$d5$ (perdeuterated form). For the 300 K simulations, 64 beads were used while 128 beads were used for all other temperatures; we note that these choices for P were made for all path integral simulations in this work. All PIMD simulations were carried out for 4 ns with a time step of 0.25 fs, starting from an initial random sampling of bead positions assuming a thermal distribution in the normal mode space of the beads. The temperature was controlled using massive Nosé-Hoover chains with a time constant of 10 fs. For classical simulations at the same temperatures, a Langevin thermostat was used with a time constant of 25 fs. For various analyses, the trajectories were saved every 250 fs in each case. The first 50 ps were treated as the equilibration time and not analysed.

From the PIMD and corresponding classical simulations at the above temperatures, distributions of internals and their average values were computed. These are defined for a property A as

$$\langle A\rangle = \left\langle \frac{1}{P}\sum_{k=1}^{P} \hat{A}(\boldsymbol{r}_1^{(k)},\ldots,\boldsymbol{r}_N^{(k)}) \right\rangle . \tag{9}$$

Choosing $\hat{A} = \hat{R}_j(\boldsymbol{r}_1,\ldots,\boldsymbol{r}_N)$, i.e. an internal from Table I, provides its PIMD average $\langle R_j\rangle$. Also of interest is the all-bead distribution of the internal $\rho(R_j)$, which is obtained by setting $\hat{A} = \delta\left(R_j - \hat{R}_j(\boldsymbol{r}_1,\ldots,\boldsymbol{r}_N)\right)$. We have analysed in particular the distributions of two main dihedrals ϕ_1 and ϕ_2 as well as distributions and averages of the OH bond lengths at various temperatures.

2. *Umbrella sampling simulations*

We have computed the free energy profiles (FEPs) along the FCCO dihedral ϕ_1 using path integral umbrella sampling (PI-US) simulations at 50 K and 300 K. Harmonic biases are applied along ϕ_1 defined using the centroids of the atoms, with centers placed every 5° in the interval from 0° to 180°. The force constants used are provided in Table S-4 (Supplementary Material). For each bias centre, PIMD simulations at both temperatures were carried out for 2FE-$h5$, 2FE-$d1$ (monodeuterated, OD only) as well as 2FE-$d5$ (perdeuterated). Corresponding classical simulations with 2FE-$h5$ were also carried out for comparison. Each simulation was 200 ps long with a time step of 0.25 fs. The distributions of ϕ_1 obtained were converted to FEPs, denoted $F_{qm;c}$, via the Weighted Histogram Averaging Method (WHAM).[63] The convergence was analysed by comparing the FEPs using data up to 150 ps versus up to 200 ps.

Although it is computationally less demanding to carry out PI-US simulations with the bias potential applied on the centroid – and has consequently been often used in literature – it is more rigorous to apply the bias to the beads:[21,24,64]

$$-\beta F_{qm;b}(\phi_1) = \ln\left[\frac{1}{P}\sum_{k=1}^{P}\langle\delta(\phi_1^{(k)} - \phi_1)\rangle\right], \tag{10}$$

where $\beta = 1/k_BT$. Direct simulations with such biases would require P independent simulations or very long simulations for a single bead. As an alternative, Lamaire et al.[64] and Cendagorta et al.[24] have shown that one can evaluate $F_{qm;b}$ using the $F_{qm;c}$ though conditional probabilities as

$$e^{-\beta F_{qm;b}(\phi_{1;b})} = \frac{\int p(\phi_{1;b}|\phi_{1;c})\, e^{-\beta F_{qm;c}(\phi_{1;c})}\, d\phi_{1;c}}{\int e^{-\beta F_{qm;c}(\phi_{1;c})}\, d\phi_{1;c}}, \tag{11}$$

where $p(\phi_{1;b}|\phi_{1;c})$ is the conditional probability of a bead having a dihedral of $\phi_{1;b}$ whenever the centroid dihedral is $\phi_{1;c}$. This can be straightforwardly obtained from the PI-US simulations by sampling the values of ϕ_1 for the beads over the various bias windows along $\phi_{1;c}$.

To complement the analyses of the free energy profiles, we have analysed the trends of various internals using Eq. (9) as well as the radii of gyration of all atoms. The latter are defined for the ith atom as

$$\mathcal{R}_{g,i}^2 = \left\langle \frac{1}{P}\sum_{k=1}^{P}\left|\boldsymbol{r}_i^{(k)} - \boldsymbol{r}_{i,c}\right|^2\right\rangle, \tag{12}$$

where $\boldsymbol{r}_{i,c}$ refers to the position of the centroid of the ith atom. The radii are a useful measure of the delocalization of nuclei and hence of NQEs along ϕ_1.

3. WTmetaD simulations

In order to capture the effect of the NQEs on the entire (ϕ_1, ϕ_2) surface, we have employed path integral well-tempered metadynamics (PI-WTmetaD) simulations on 2FE. These were carried out by interfacing our simulation code with PLUMED 2.8.0.[22,62,65] Using ϕ_1 and ϕ_2 as the two collective variables (CVs), long simulations of 45 ns with 0.25 fs time steps were performed for the normal and perdeuterated forms of 2FE at both 300 K and 50 K. Classical simulations of 75 ns duration were carried out with the normal form of 2FE at both temperatures. At 300 K, Gaussians with widths of 0.1 and 0.3 rad along ϕ_1 and ϕ_2, respectively, were deposited once every 500 steps. These were lowered to 0.05 and 0.1 rad at 50 K with a deposition once every 300 steps. The Gaussian widths were chosen as about one-third of the widths of the distributions around the G^+g^- basin of both dihedrals from unbiased simulations at the corresponding temperatures. The Gaussian heights were initialized at 1.2 kJ/mol (0.2 kJ/mol) at 300 (50) K, which are roughly $k_BT/2$. In WTmetaD, the height of the deposited Gaussian decreases over time, which was monitored as one of the measures of the sufficiency of the simulation length. We have used metadynamics bias factors[59] $\gamma = 120$ (20) at 50 K (300 K). By providing high effective temperatures, γ improves the coverage in the dihedral space. Using PLUMED,[62] the free energy surfaces were computed in (ϕ_1, ϕ_2) space. Convergence of the surfaces were checked with block averaging analyses using the last several ns of the simulations.

4. T-RPMD simulations

The role of NQEs on the infrared spectra of 2FE were analysed with thermostatted ring polymer molecular dynamics (T-RPMD) simulations[56] at 50 K and 300 K. The path integral Langevin thermostat (PILE) was applied on the non-centroid modes. We have also used the Cayley transform-based modification for the T-RPMD simulation recently proposed by Miller and coworkers.[66,67] This approach provides strong stability to the equations of motion and also allows for larger time steps. Based on their study, the BCOCB scheme is used (B: half-step momemtum update due to external potential; C: half-step Cayley-modified integration for the harmonic motion of the free ring polymer; O: thermostat on non-centroid modes for the full time step). A total of 53 and 52 initial conditions at 50 K and 300 K, respectively, were sampled every 10 ps from long PIMD trajectories. Each T-RPMD trajectory was 100 ps long with a timestep of 0.5 fs. Counterpart classical simulations at both temperatures were carried out from 100 initial geometries, each for a total time of 100 ps with 0.25 fs timesteps. In all cases, the trajectory was saved every 1 fs. The infrared spectrum was calculated using the dipole moment surface for 2FE developed in this work. The bead averaged dipole moment was computed at a given time step as[5,10]

$$\boldsymbol{\mu}_P(t) = \frac{1}{P}\sum_{k=1}^{P} \boldsymbol{\mu}(\boldsymbol{r}_1^{(k)}, \ldots \boldsymbol{r}_N^{(k)}). \tag{13}$$

The correlation function $C_{\mu\mu}(t) = \langle \boldsymbol{\mu}_P(0) \cdot \boldsymbol{\mu}_P(t) \rangle$ was computed with $\Delta t = 1$ fs and averaged over simulations. No damping was applied. Fourier transformation of the correlation function using 2^{14} steps (~ 1 cm^{-1} resolution) yielded the spectrum.

III. RESULTS AND DISCUSSION

A. PES fit and quality

Figure 2 shows the relaxed ab initio dihedral surface for 2FE at a grid of (ϕ_1, ϕ_2) points with 15° step sizes along both dihedrals. As V_{rc} is even (see Eq. (3)), only half the points need to be computed. Along with the special points in Table I, a total of 294 unique (ϕ_1, ϕ_2) points are used. The figure shows that the starting from G$^+$g$^-$, the barriers to G$^+$t and further to G$^+$g$^+$ are lower ($\sim 750 - 1000$ cm^{-1}) than the those to access the Tx basins, x=g$^\pm$,

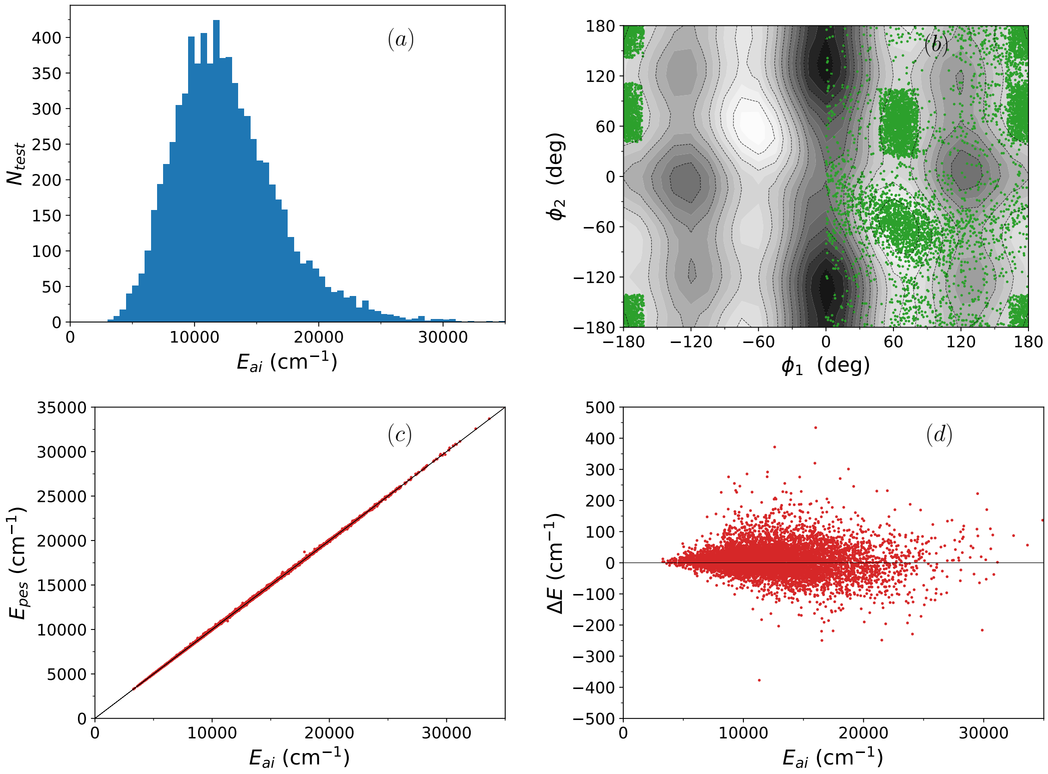

FIG. 3. Accuracy of the full dimensional PES for 2FE against a test set of 7479 points. (a) Distribution of ab initio (MP2/aVTZ) energies at the test points. (b) Distribution of the test points in (ϕ_1, ϕ_2) space. (c) Comparison of fitted and ab initio energies. (d) Signed error, $\Delta E = E_{fit} - E_{ai}$, as a function of the ab initio energies of the test points. (Note: one test point at ~ 18000 cm^{-1} with an error of ~ 800 cm^{-1} is not shown in (d).)

TABLE III. List of (M_{max}, N_{max}) values for the dihedral expansion of various potential terms in 2FE; see Eqs. (4) and (5). For cubic and quartic terms, the expansion sizes were chosen based upon the size of the *variation* of the term as a function of the dihedrals, defined as $\Delta f = f_{max}(\phi_1, \phi_2) - f_{min}(\phi_1, \phi_2)$.

Term		(M_{max}, N_{max})
V_{rs}		(8,6)
$\boldsymbol{S}^\circ$		(8,6)
$f^{(2)}$		(8,6)
$f^{(3)}$, $f^{(4)}$	$\Delta f \geq 5$ cm^{-1}	(8,6)
	$2 \leq \Delta f < 5$ cm^{-1}	(6,6)
	$0.1 \leq \Delta f < 2$ cm^{-1}	(5,5)
	$\Delta f < 0.1$ cm^{-1}	const
$f^{(5)}$-$f^{(8)}$		(3,3)

TABLE IV. Accuracy of the MP2/aVTZ+DZ-based PES for 2FE, measured using MP2/aVTZ energies and forces at 7479 test data points. In addition to energies and forces, the comparison of force magnitudes and angle between the ab initio and fitted force vectors is also provided. The force errors are defined in Eq. 14.

		Full		Quartic	
		RMSE	MAE	RMSE	MAE
E	cm^{-1}	49.3	33.4	422.2	157.6
F_{abs}	cm^{-1}/Å/dof	269.8	160.7	1785.8	464.0
F_{mag}	cm^{-1}/Å/atom	63.7	44.8	791.7	335.9
$\alpha_{ab,fit}$	deg	0.85	0.75	3.02	1.79

t ($\sim$1500 cm^{-1}). Direct conversion of G^+ to G^- can occur via the Cc transition state, which offers the highest barrier of about 2500 cm^{-1}. The plot suggests that OH dihedral motion can be expected to be more vigorous than FCCO.

The 294 dihedral points are fitted using Eq. (2) with $(M_{max}, N_{max}) = (8, 6)$, yielding an RMSE (MAE) of 0.56 (0.44) cm^{-1}. Given the high accuracy, the contour plot of the fitted V_{rs} is indistinguishable from the ab initio plot of Figure 2 (and hence not shown here). Additionally, optimized and symmetrized internals $\boldsymbol{S}^{\circ}$ were also fitted to even or odd expansions (Eqs. (4) and (5)) as appropriate using $(M_{max}, N_{max}) = (8, 6)$, yielding accurate fits. For example, the RMSE (MAE) of the fit with 294 points for S_8° ($\equiv r_{\mathrm{OH}}$) was obtained as 8.1×10^{-6} (5.6×10^{-6}) Å, while that for S_{15}° ($\equiv \theta_{\mathrm{COH}}$) was found to be 0.0023° (0.0018°). The full list of RMSE and MAE values for all internals is given in Table S-3.

For terms in V_b, the expansion sizes used are collected in Table III. All quadratic terms are expanded with $(M_{max}, N_{max}) = (8, 6)$. The same size was also used for cubic and quartic terms whose variation in dihedral space, defined as $\Delta\tilde{f} = \tilde{f}_{max}(\phi_1, \phi_2) - \tilde{f}_{min}(\phi_1, \phi_2)$, was larger than 5 cm^{-1}. This set of terms includes several one- and two-body terms of large magnitude. For terms whose variation was smaller, several lower expansion sizes were attempted and the ones listed in Table III were found optimal. Note that terms with too low a variation (0.1 cm^{-1}), which typically constitutes terms of small or very small magnitudes, were treated as constants. Lastly, for the quintic-octic terms, expansions with $(M_{max}, N_{max}) = (3, 3)$ were found sufficient. Note also that the ab initio data for the quadratic terms is at the MP2/aVTZ level while the rest are at the MP2/aVDZ level, as explained in Sec. II B

To measure the quality of the full dimensional PES, a test set of ab initio points was prepared with the following approach. From long PIMD simulations at 300 K with the potential truncated up to quartic terms, geometries of selected beads (every 16th) were sampled at 0.5 ps intervals. The sample points were mainly in the $\mathrm{G}^+\mathrm{g}^-$ basis, but a small fraction were also from the G^+t and $\mathrm{G}^+\mathrm{g}^+$ regions. The sample points were filtered based on proximity. To this end, vectors composed of bond distances, bond angles and dihedrals are constructed for each geometry. From these, magnitudes of difference vectors between different geometries was calculated. Denoting these as l_b, l_a and l_d for a pair of geometries, it was ensured that at least two of the following criteria were satisfied: $l_b > 0.2$ Å, $l_b > 5°$ and $l_d > 15°$. A total of 1077 sample points were selected in this manner.

In order to sample points at other minima that are not accessed by PIMD, we have employed a sampling approach due to Brown[68] that is based on the quantum harmonic distribution (QHD). At each minimum of 2FE, the quantity $d(\tilde{\nu}_i, A) = h/(8\pi^2 c\tilde{\nu}_i)\coth(1/2A)$, where c is the speed of light, provides the variance for ith mode with frequency $\tilde{\nu}_i$ (in cm^{-1}). If $A = k_B T/hc\tilde{\nu}_i$, the exact QHD is obtained. However, A is treated as a dimensionless parameter here. The variances along all modes at a given minimum are used in a multidimensional Gaussian distribution to obtain random displacements in all normal modes, thereby generating sample geometries. By varying A, the spread of the distribution can be controlled. As shown by Brown,[68] using A instead of temperature T has two related advantages. First, the sampling of low frequency modes is on a par with that for high frequency modes. Second, to generate sufficiently displaced high frequency modes, high T needs to be used. But this generates overly distorted geometries in low frequency modes. Such a problem is avoided by using suitable values of A instead. Following Brown, we have used $A = 0.5$, 1 and 2, and obtained geometries at the Tt, Tg$^+$ and G$^+$g$^+$. The selected geometries are such that (1) no internal is excessively displaced; geometries were discarded if $|R_i - \langle R_i \rangle| > 1.5\sigma(R_i)$, where the mean $\langle R_i \rangle$ and standard deviation $\sigma(R_i)$ were estimated from the PIMD simulation with the quartic potential, and (2) the chosen points satisfied the same geometric non-proximity criteria as used for the PIMD sampling. A total of 4500 points (500 points per A value per minimum) were selected in this manner.

Additional points were sampled to cover other regions of the (ϕ_1, ϕ_2) landscape away from the minima and not already covered by the PIMD sampling. For this, we took samples of points in selected regions from the umbrella sampling simulations along ϕ_1 amounting to 1402 points. From the last 3 ns of the classical 300 K WT-metaD simulations, an additional points of 500 point were sampled. In the selection of these points, it was ensured that the points are sufficiently apart from each other using the bond distance, angle and dihedral criteria discussed above.

A combined test set of 7479 geometries are thereby obtained. Ab initio energies and forces are computed at the MP2/aVTZ level. Figure 3(a) shows the spread of the sampled points in energy. The peak of the distribution is close to the ZPE of 2FE. Part (b) of the figure shows the distribution of the test points in (ϕ_1, ϕ_2) space. Owing to the symmetry, one half of the space was not sampled. The comparison of the test set energies data to those obtained with the fitted, MP2/aVTZ+DZ based potential at the same geometries is provided in Figures 3(c) and (d) and Table IV. The former shows that errors at most points lie within ±200 cm^{-1}. Geometries close to the centre of the distribution are displaced along many modes leading to the observed error. However, geometries with large ab initio energies are likely to have dominant displacements in one or two modes, and their errors are evidently smaller. Quantitative comparisons in Table IV using RMSEs and MAEs for the energies and forces attest to the accuracy of the potential. The force errors are defined[69] as

$$\begin{aligned} F_{abs} &= \frac{1}{3N} \sum_{i=1}^{N} \sum_{\alpha=x,y,z} |F_{i\alpha;\,fit} - F_{i\alpha;\,ai}| \\ F_{mag} &= \frac{1}{N} \left(|\boldsymbol{F}_{ai}| - |\boldsymbol{F}_{fit}|\right) \\ \alpha_{ab,fit} &= \cos^{-1}(\boldsymbol{F}_{ai} \cdot \boldsymbol{F}_{fit}/|\boldsymbol{F}_{ai}||\boldsymbol{F}_{fit}|), \end{aligned} \tag{14}$$

TABLE V. Errors in fitted atomic charges (in a.u.) at the 294 (ϕ_1, ϕ_2) geometries. Fits are carried out with (M_{max}, N_{max}) = (10,8).

Atom	MAE ($\times 10^{-3}$)	RMSE ($\times 10^{-3}$)
C_1	2.56	3.58
C_2	2.43	3.60
O_3	0.49	0.65
F_4	0.54	0.73
H_5	0.80	1.14
H_6	0.79	1.12
H_7	0.82	1.15
H_8	0.78	1.07
H_9	0.27	0.33

TABLE VI. Comparising of the fitted $\boldsymbol{\mu}_{rs}$ to the ab initio dipole moment on the dihedral surface. All quantities are in a.u.

	MAE ($\times 10^{-4}$)	RMSE ($\times 10^{-4}$)
μ_x	0.629	7.818
μ_y	1.623	2.006
μ_z	1.792	2.205

where $\boldsymbol{F}_{fit/ai}$ are the force vectors obtained from the PES and ab initio calculations. The table also shows the need to introduce the quintic-octic terms in bond distances and angles; there is a marked improvement in the PES quality with these terms. (See also Fig. S-1 for a graphical representation of the errors for the quartic PES.)

As the aim of this work is the exploration of NQEs for 2FE with path integral simulation, it is important to obtain a PES that is accurate at large displacements that are typically accessed by beads in such simulations. The results presented above suggest that our MP2/aVTZ+DZ based fitted PES is suitable for the objective. The PES is available on Github; see the Supplementary Material section below.

B. DMS fits

Table V shows the quality of the fit to the atomic charges for 2FE using HLY charges at 294 reaction surface points. The fits used $(M_{max}, N_{max}) = (10, 8)$. Using the fitted charges, the dipole moments on the reaction surface are compared with ab initio dipole moments componentwise in Table VI. Finally, Table VII provides a comparison of the $\boldsymbol{\mu}_b$ part of the dipole expansion at the displaced geometries from the reaction surface (see Sec. II C). Overall, the fits are found to be satisfactory.

TABLE VII. Comparison of the dipole moments at geometries displaced from the dihedral surface (see Sec. II C). Large displacements refer to ±0.03 and ±0.04 Å in bonds and ±1.5° and ±2.0° in angles and dihedrals, while small displacements are ±0.002 Å and ±0.004 Å in bonds and ±0.1° and ±0.2° in angles and dihedrals. All errors are reported in a.u.

	MAE ($\times 10^{-4}$)			RMSE($\times 10^{-4}$)		
	$\Delta\mu_x$	$\Delta\mu_y$	$\Delta\mu_z$	$\Delta\mu_x$	$\Delta\mu_y$	$\Delta\mu_z$
Small displ	0.653	1.642	1.819	8.255	2.033	2.245
Large displ	1.322	2.811	3.215	3.125	4.195	5.214
Overall	0.988	2.227	2.517	2.285	3.297	4.015

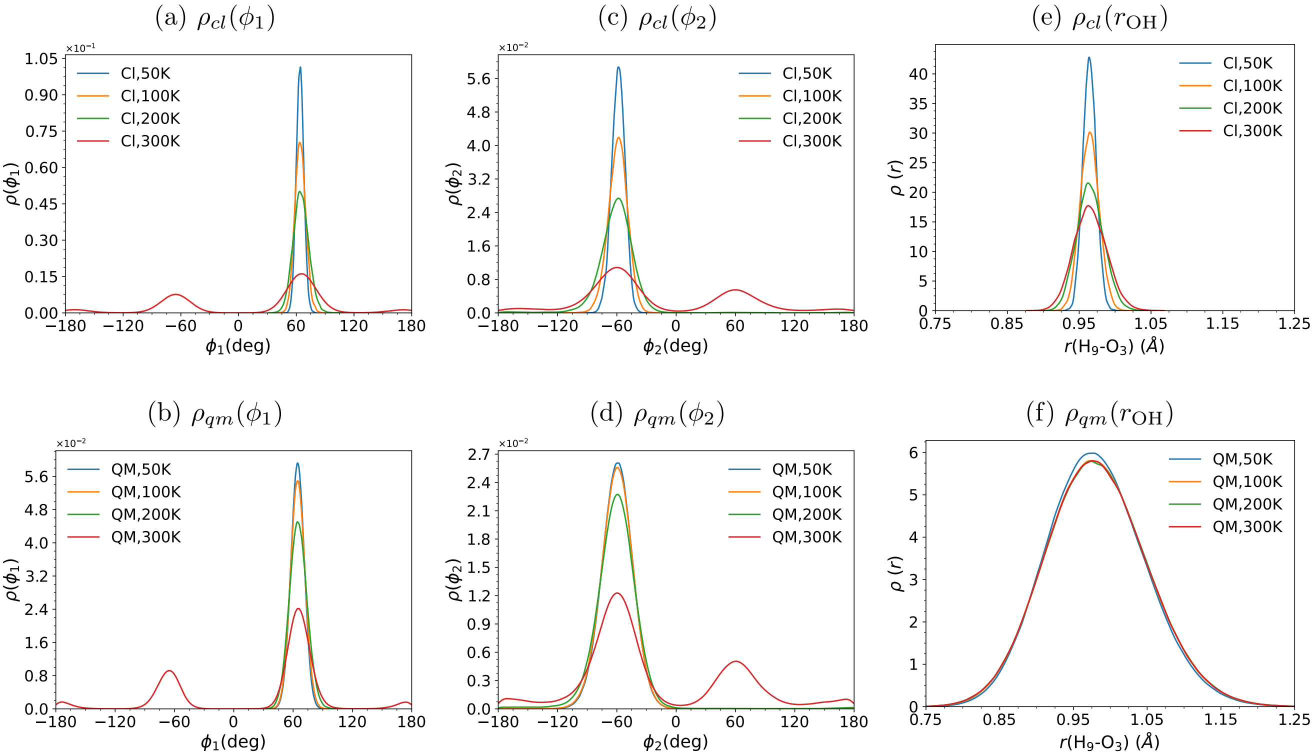
(a) $\rho_{cl}(\phi_1)$ (c) $\rho_{cl}(\phi_2)$ (e) $\rho_{cl}(r_{\mathrm{OH}})$

(b) $\rho_{qm}(\phi_1)$ (d) $\rho_{qm}(\phi_2)$ (f) $\rho_{qm}(r_{\mathrm{OH}})$

FIG. 4. Distributions of the (a, b) FCCO (ϕ_1) and (c, d) CCOH (ϕ_2) dihedrals as well as the (e, f) OH bond length (r_{OH}) from (a, c, e) classical and (b, d, f) PIMD simulations of 2FE-$h5$ at various temperatures.

C. PIMD simulations

As a first assessment of the NQEs in 2FE, we present the distributions of the FCCO (ϕ_1) and CCOH (ϕ_2) dihedrals and the OH bond length from classical and PIMD simulations at various temperatures in Fig. 4. The simulations were initiated in the G^+g^- basin.

The plot for $\rho_{cl}(\phi_1)$ in Fig. 4(a) shows narrow classical distributions. The widths increase with temperature as more energy is available to sample a larger ϕ_1 range. The all-bead

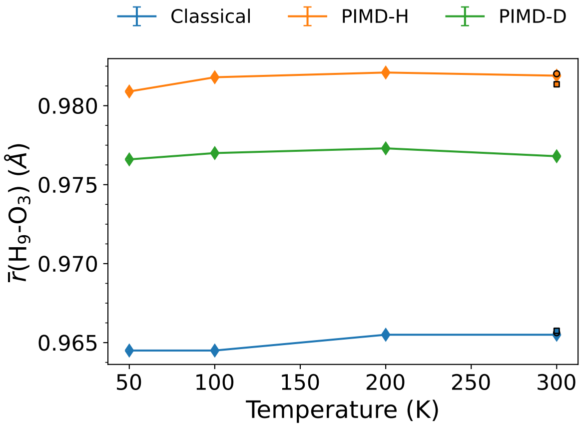

FIG. 5. Trends of the average OH and OD distances as a function of temperature from classical and PIMD simulations of 2FE-*h*5 and 2FE-*d*5. The sizes of the points correspond to the error bars derived from block-averaging at that temperature. Shown also for 300 K are the values of the OH distance for geometries in the G^+g^- and G^-g^+ minimum basins (circles) and Tt (squares) for PIMD and classical simulations with 2FE-*h*5. Similar plots for other selected internals are given in Fig. S-2.

quantum distributions $\rho_{qm}(\phi_1)$ at various temperatures, shown in Fig. 4(b), are clearly wider than their classical counterparts. Note also that the 50 K and 100 K distributions nearly the same. This is because these temperatures are lower than the ZPE of this mode ($\sim$75 cm^{-1}) and NQEs result in an almost temperature independent distribution over this range. At higher temperatures, when the available energy exceeds the ZPE, thermal effects are evident. The classical and quantum 300 K distributions span the other conformers, i.e. G^- and T. The trajectories show that the G^- region is accessed from G^+ through the T region, which has a relatively lower barrier compared to a direct crossover; see Fig. 2. As the G^+ and G^- are equivalent conformers, the peak heights of the distributions shown are expected to be the same; we attribute the observed difference to be due only to the finite trajectory length used. It should be pointed out that the G^+ to T to G^- transitions are still rare on the timescale of the simulation and the residence times in the gauche basins along ϕ_1 are large.

Fig. 4(c,d) contrast the classical and quantum distributions for ϕ_2. As the frequency of this mode is roughly double that of ϕ_1, the effects of temperature are small until 200 K. At 300 K, it is evident that the g^+, g^- and t regions are sampled. We note that the peak heights of the g^+ and g^- regions of $\rho(\phi_2)$ are different. This is an artifact of the ϕ_1 sampling described above; to the extent that G^+ and G^- regions are not equally sampled due to finite simulation length, the populations in the g^+ and g^- regions would also be expected to be different.

Of special interest are NQEs on the OH bond distance as well as the OF and HF distances and OHF angle, which are markers of intramolecular interactions involving of the O-H and F groups of 2FE. The distributions in Fig. 4(e,f) show the classical and quantum $\rho(r_{OH})$, respectively. While the classical distributions are again narrow and a function of

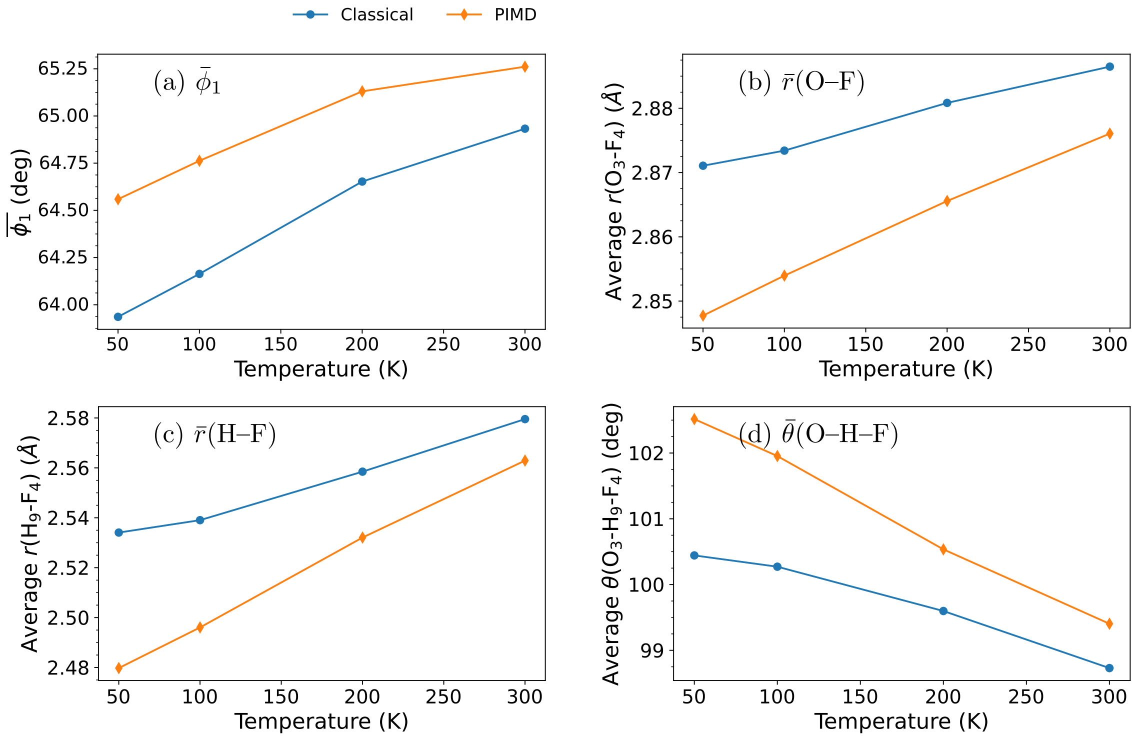

FIG. 6. Averages of (a) ϕ_1, (b) r(O-F), (c) r(H-F) and, (d) θ(O-H-F) as a function of temperature for geometries restricted to the G$^+$g$^-$ and G$^-$g$^+$ minima.

temperature, the quantum counterparts are essentially invariant with temperature since the thermal energies are much lower than the ZPE for this mode. Fig. 5 shows the average r_{OH} from these distributions as a function of temperature. (Averages of other selected internals is given in Fig. S-2.) The classical $\bar{r}_{\mathrm{OH}}$ is close to the G$^+$g$^-$ equilibrium distance at low temperatures and slightly increases at higher temperatures. The PIMD simulations show expectedly larger averages for both OH (2FE-*h*5) and OD (2FE-*d*5) bond distances, with a small temperature variation. The elongation between classical and quantum simulations is significant, about 16-17% of the zero-point the amplitude of the OH or OD bond, respectively. However, this effect is also seen for the CH stretches (Fig. S-2) and hence is essentially due to the anharmonicity of the high frequency stretch modes at their ZPEs.

The observations above for r_{OH} also hold true for trajectory points in the global minimum region alone. This is achieved by considering only the points in the G$^+$g$^-$ ($30° \leq \phi_1 \leq 90°$ and $-120° \leq \phi_2 \leq 0°$) and G$^-g^+$ ($-30° \geq \phi_1 \geq -90°$ and $120° \geq \phi_2 \geq 0°$) basins. The classical and quantum distribution for r_{OH} so obtained (not shown) are practically indistinguishable from those in Figs. 4(e) and (f). In Fig. 5, the circles indicate the averages for r_{OH} limited to the G$^+$g$^-$ and G$^-$g$^+$ minima at 300 K, which are very close to unrestricted average. (Note that at lower temperatures the classical and quantum simulations do not sample the trans basin for ϕ_1; see Figs. 4(a,b).) Also indicated with squares are the averages of the bond length for the Tt geometry. From PIMD simulations, this value is very slightly (less than 0.001 Å) smaller than the value in the minimum basin. This suggests that, in the global minimum region, the OH stretches show at best a weak NQE due to interaction with the F atom.

Shown in Fig. 6 are the trends of ϕ_1, the OF and HF distances and OHF angle in the global minimum basins as a function of temperature for 2FE-$h5$. At each temperature, the PIMD average $\bar{\phi}_1$ is slightly larger by 0.5-0.6° compared to the classical average. The PIMD average distances, $\bar{r}_{\rm OF}$ and $\bar{r}_{\rm HF}$, are slightly smaller while $\bar{\theta}_{OHF}$ average angle is slightly larger than the correponding classical MD averages at each simulated temperature. The changes for these three marker variables between PIMD and classical simulations suggests that zero point effects promote a weak favourable interaction between the OH and F groups at all temperatures.

The all-bead distributions of ϕ_1, $r_{\rm OF}$, $r_{\rm HF}$ and θ_{OHF} in the global minimum basins at various temperatures are shown in Fig. S-3. The classical distributions are expectedly narrow at low temperatures, but approach the quantum distributions at high temperature. In particular, the classical and quantum $\rho(\phi_1)$ are almost the same at 300 K. As the OF and HF distances are a function of ϕ_1, their distributions follow that of ϕ_1. The OHF angle is evidently somewhat less modulated by ϕ_1; its quantum distribution is seen to be less affected by temperatures over simulated range.

Note also that all distributions are only not broader but more asymmetric at higher temperatures. Those for the $r_{\rm OF}$ and $r_{\rm HF}$ are wider towards larger distances at high temperatures, while that for $\theta_{\rm OHF}$ is wider towards smaller angles. These mirror the distributions of ϕ_1 itself and suggest that the average distances (angle) would be higher (smaller) for larger temperatures. Indeed, this is the temperature trend seen in Fig. 6, which occurs as an indirect consequence of the temperature effects on ϕ_1 in both classical and quantum simulations.

Though the temperature trends on the marker variables can be rationalized as above, it must be stressed that the NQE magnitudes reported by them for the interaction between the OH and F groups is still very small. This is further emphasized from the umbrella sampling results on the same set of variables, discussed later in Sec. III E.

D. PI-WTmetaD simulations

A direct view of the quantum effects in (ϕ_1, ϕ_2) space can be obtained via metadynamics simulations using the dihedral pair as the collective variables. We note that centroid-based dihedrals were used for these calculations and the free energy surfaces (FES) so obtained are noted $\Delta F_{qm;c}(\phi_1, \phi_2) = F_{qm;c}(\phi_1, \phi_2) - F^{min}_{qm;c}$. The c suffix indicates the use of centroids for adding biases during the simulation.

Fig. 7(a) shows the FES obtained from well-tempered metadynamics simulations at 50 K for 2FE-$h5$, while part (b) shows the differences between the 50 K and 300 K surfaces. While $\Delta F^{50K}_{qm;c}$ is qualitatively similar to $V_{rs}(\phi_1, \phi_2)$ (compare Fig. 2), the differences between the two are highlighted in part (c) of the figure. The FES is lower than the PES by up to a few hundred cm^{-1} in the barrier regions. In particular, the Cc barrier energy is lowered by about 150 cm^{-1}.

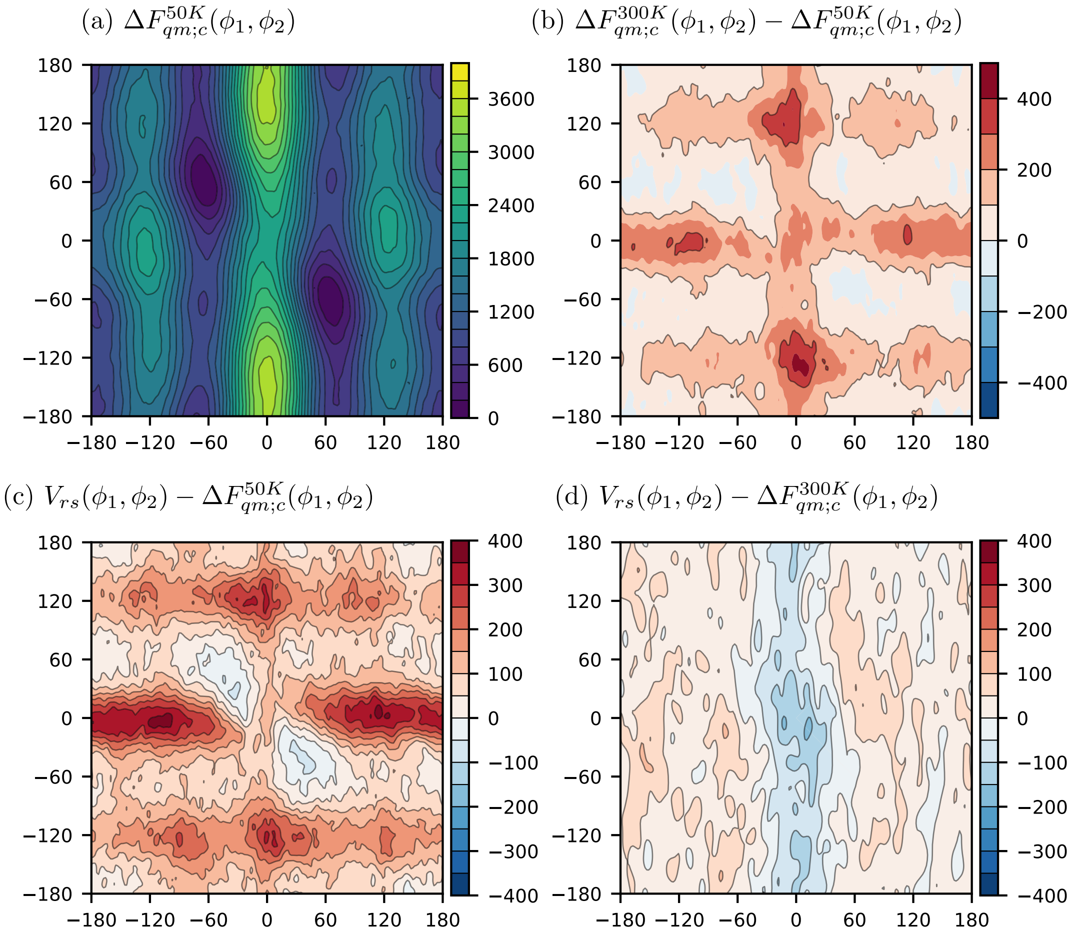
(a) $\Delta F^{50K}_{qm;c}(\phi_1, \phi_2)$

(b) $\Delta F^{300K}_{qm;c}(\phi_1, \phi_2) - \Delta F^{50K}_{qm;c}(\phi_1, \phi_2)$

(c) $V_{rs}(\phi_1, \phi_2) - \Delta F^{50K}_{qm;c}(\phi_1, \phi_2)$

(d) $V_{rs}(\phi_1, \phi_2) - \Delta F^{300K}_{qm;c}(\phi_1, \phi_2)$

FIG. 7. Free energy surfaces in (ϕ_1, ϕ_2) space at 50 K and 300 K obtained from PI-WTmetaD simulations and their differences with respect to the $V_{rs}(\phi_1, \phi_2)$. Shown are (a) the free energy surface at 50 K, and the differences between (b) 300 K and 50 K surfaces, (c) V_{rs} and 50 K surfaces, and (d) V_{rs} and 300 K surfaces. The contour scales are in cm^{-1}.

Fig. 7(d) contrasts the PES with the FES at 300 K. The differences are small everywhere (± 100 cm^{-1}), including near $\phi_1 = 0°$, where the FES is higher than the PES by about 100 cm^{-1}. This corroborates the similarity in the difference patterns seen in parts (b) and (c) of the figure. Overall, this suggests that through centroid-based biased simulations, small quantum effects are found at low temperatures.

E. PI-US simulations

With barriers along the FCCO torsion being higher, we have explored the free energy surfaces along this coordinate via path integral umbrella sampling simulations with a view to carrying out a detailed analysis of NQEs. We first present results obtained with harmonic biases applied to the centroid $\phi_{1;c}$, the parameters for which are given in Table S-4 for both

(a) 50 K and 300 K

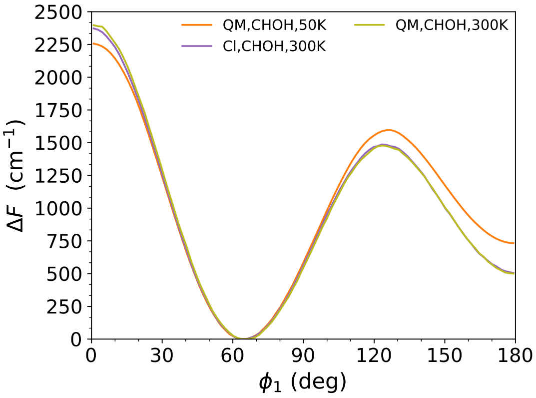

(b) H/D isotopic variation at 300 K

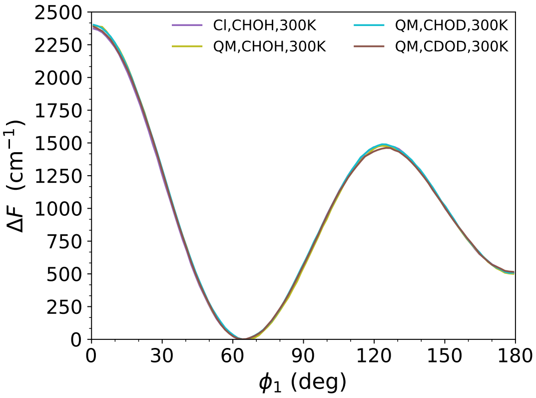

(c) H/D isotopic variation at 50 K

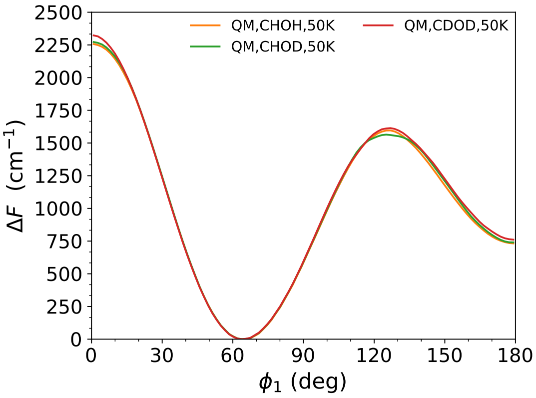

FIG. 8. Centroid-biased free energy profiles, $\Delta F_{qm;c}(\phi_1) = F_{qm,c}(\phi_1) - F_{qm,c}^{min}$, at various temperatures obtained by path integral umbrella sampling simulations along ϕ_1. Classical simulation results are shown alongside. **(a)** A comparison of profiles at 50 K and 300 K for 2FE-*h*5. **(b)** Variation of $F_{qm;c}(\phi_1)$ with isotopic substitutions, 2FE-*d*1 and 2FE-*d*5, at 300 K. **(c)** Same as (b) but at 50 K. Notation: CHOH $\equiv$ 2FE-*h*5, CHOD $\equiv$ 2FE-*d*1, CDOD $\equiv$ 2FE-*d*5.

50 K and 300 K simulations. Fig. 8 shows the free energy profiles (FEPs) $\Delta F_{qm;c}(\phi_1) = F_{qm;c}(\phi_1) - F_{qm;c}^{min}$ along with their classical counterparts.

(a) $\Delta F_{qm;b}$ vs. $\Delta F_{qm;c}$

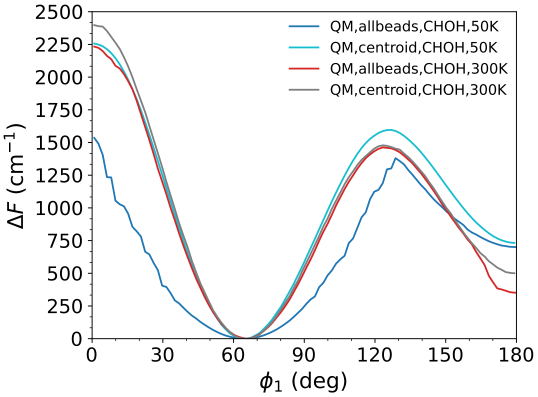

(b) $\Delta F_{qm;b}$ with H/D isotopic substitutions

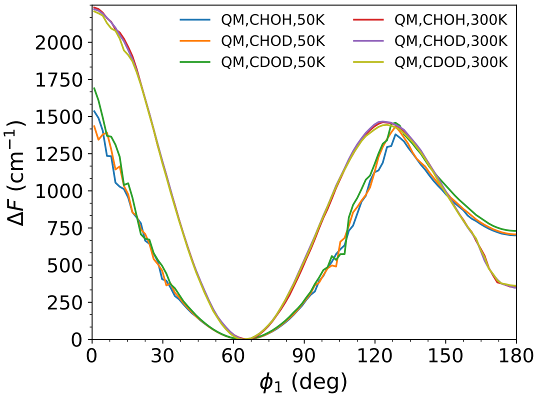

FIG. 9. Bead-biased free energy profiles $\Delta F_{qm;b}(\phi_1) = F_{qm;b}(\phi_1) - F_{qm,b}^{min}$, obtained using Eq. 11. **(a)** Comparison with centroid-based $F_{qm;c}$ profiles at 50 K and 300 K for 2FE-*h*5. **(b)** Bead-biased FEPs for various H/D isotopic substitutions at 50 K and 300 K. Notation: CHOH $\equiv$ 2FE-*h*5, CHOD $\equiv$ 2FE-*d*1, CDOD $\equiv$ 2FE-*d*5.

We first analyse the FEPs for 2FE-*h*5 in Fig. 8. Part (a) of the figure shows that over a wide ϕ_1 range spanning about 25°-100°, which encompasses the G^+ minimum, all FEPs are essentially identical. (50 K classical simulation results are not shown due to convergence issues; see below and the caption of Table S-4.) Differences are visible near the C conformer ($\phi_1 = 0°$) and also at and beyond the G^+-T barrier ($\phi_1 \sim 120°$). In the former region, only the 50 K PIMD curve stands out as having a slightly lower barrier than the other quantum and classical FEPs, all of which show essentially the same barrier.

However, the $F_{qm;c}$ trends appear reversed for $\phi_1 \gtrsim 100°$. The energy of the T minimum ($\phi_1 = 180°$) relative to the G^+ is higher at 50 K. This is also true for the barrier around $\phi_1 = 120°$. A partial explanation of the effect is suggested by the presence of two equienergetic local basins at $\phi \sim 120°$ with $\phi_2 \sim -80°$ and $-180°$, respectively, that are separated by a barrier around $\phi_2 = 135°$; see Fig. 2). PIMD trajectories at 50 K in this region show that infrequent jumps occur between these two basins, necessitating lower umbrella sampling force constants and with higher simulation time. (Note that 50 K classical results are not shown owing to insufficient sampling in this region yielding an unconverged FEP.) In contrast, the

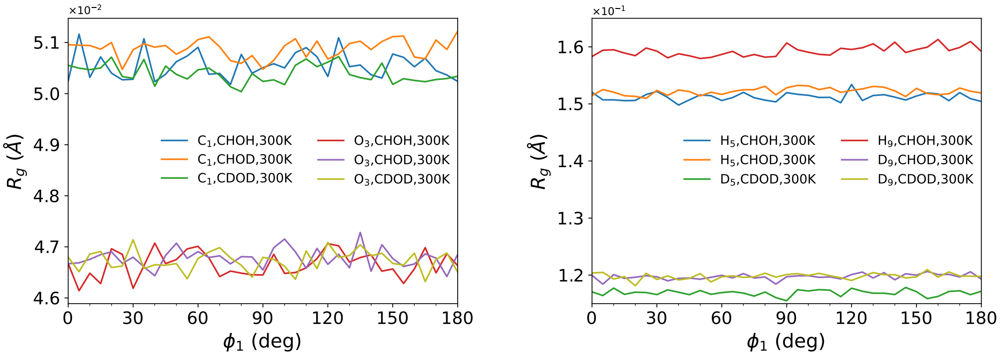

(a) 300 K, $\mathcal{R}_g(\mathrm{C},\mathrm{O})$ (b) 300 K, $\mathcal{R}_g(\mathrm{H_{CH}},\mathrm{H_{OH}})$

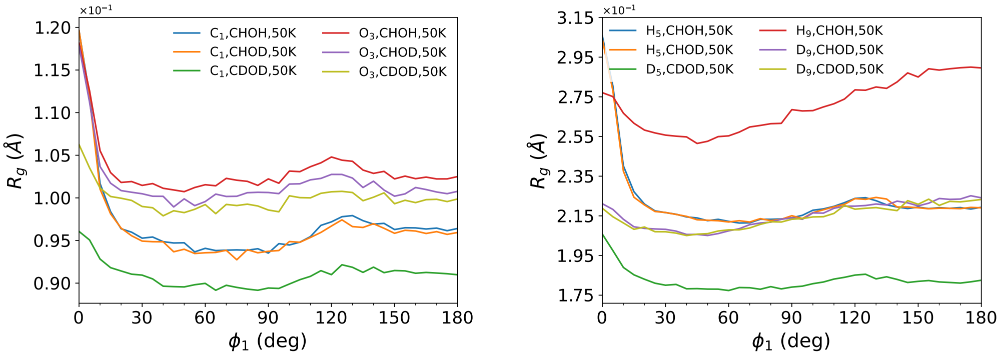

(c) 50 K, $\mathcal{R}_g(\mathrm{C},\mathrm{O})$ (d) 50 K, $\mathcal{R}_g(\mathrm{H_{CH}},\mathrm{H_{OH}})$

FIG. 10. Mean radii of gyration $\mathcal{R}_g$ of atoms in 2FE-$h5$, 2FE-$d1$ and 2FE-$d5$ as a function of ϕ_1 at both (a, b) 300 K and (c, d) 50 K. Shown in (a) and (c) are the radii of the carbon and the oxygen atoms, while those in (b) and (d) are the radii of the CH and OH hydrogens. See Fig. 1 for the atom numbering.

traversals between the local basins are more frequent at 300 K. Corroborating this analysis is the distribution of ϕ_2 at various ϕ_1 values for the centroid along the umbrella sampling path, shown in Fig. S-4 (Supplementary Material). The spread of ϕ_2 is lower around $\phi_1 \sim 120°$ at 50 K compared to 300 K. In fact, this trend continues until 180° as well. These observations suggest differences in the FEPs at the two temperatures due to varying extents of access to different regions of torsional space.

Fig. 8(b) and (c) compares $F_{qm;c}(\phi_1)$ for 2FE-$d1$ and 2FE-$d5$ at 300 K and 50K. There is evidently no significant difference due to isotopic substitution at 300 K. At 50 K as well, the plots are mostly similar, except near the C conformer. In this region, the $F_{qm;c}$ barrier increases in the order 2FE-$h5$, 2FE-$d1$, and 2FE-$d5$, while the fully classical simulations show the highest barrier. Although the differences are small (the barrier height for quantum and classical 2FE-$h5$ differ by ~ 125 cm^{-1}), it is significant that deuterating the OH hydrogen only slightly raises the barrier, while deuterating all four CH hydrogens yields a larger change.

As noted in Sec. II D 2, $F_{qm;b}$ obtained from applying harmonic bias to the beads rather than the centroid better encapsulates NQEs. Following recent work,[24,64] we have used Eq. 11 to compute it using $F_{qm;c}$. Fig. 9(a) compares both types of FEPs at 300 K and 50 K. At

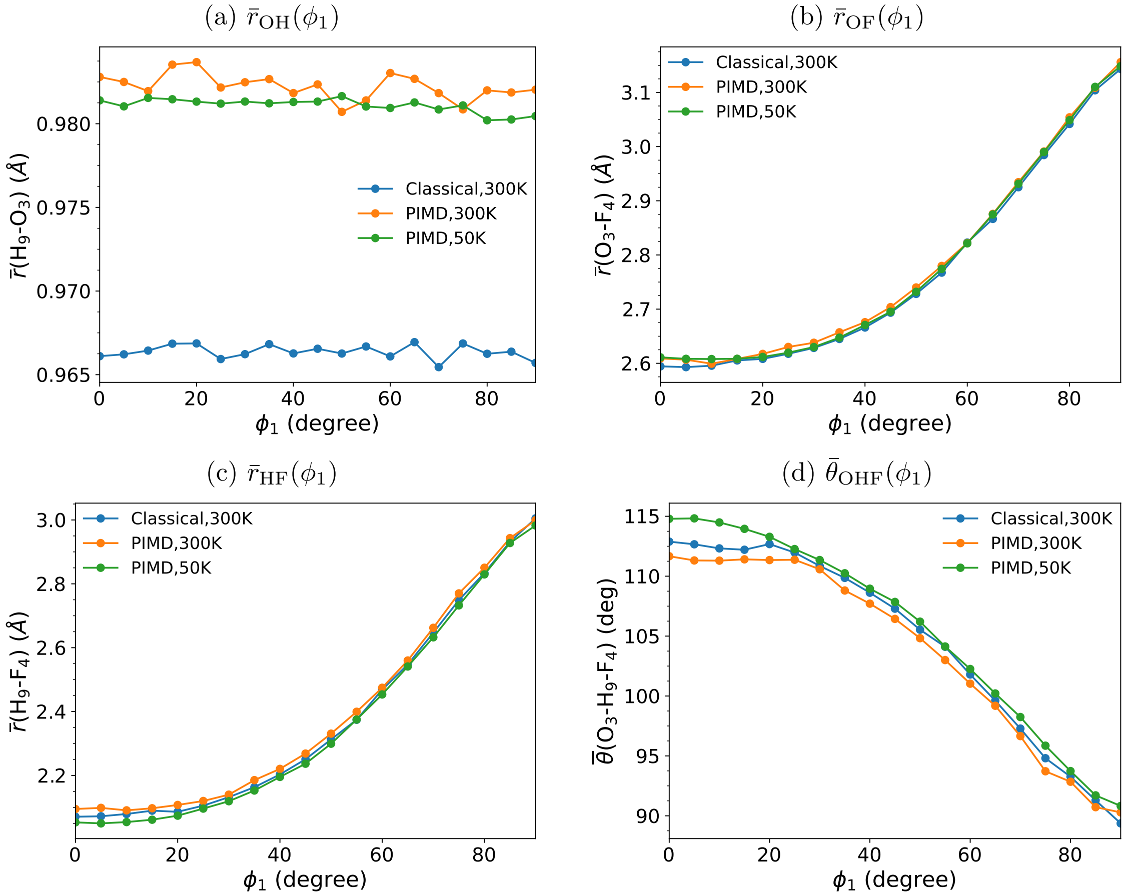

FIG. 11. Averages of the distributions of the (a) OH, (b) OF and (c) HF distances and the (d) OHF angle as a function of ϕ_1 for geometries obtained from umbrella sampling. The corresponding trends of standard deviations of the distributions are provided in Fig. S-7. For the analyses, only those geometries with $-120° \leq \phi_2 \leq 0°$ for $\phi_1 > 30°$ and $-60° \leq \phi_2 \leq 60°$ for $\phi_1 < 30°$ are considered; see Fig. S-4 for the (ϕ_1, ϕ_2) distributions.

the higher temperature, the two FEPs are very similar, except for ϕ_1 near 0° and near 180°. In contrast, $\Delta F_{qm;b}$ is much lower than $\Delta F_{qm;c}$ at 50 K. In particular, the $\phi_1 = 0°$ barrier is strongly reduced from $\sim$ 2250 cm^{-1} to $\sim$ 1500 cm^{-1}, pointing to a significant NQE in this region. Also, the G$^+$-T barrier for 50 K is lower than that for 300 K. Compared to the behaviour of the centroids (see above), the beads are well-delocalized. We note that torsional G$^+$-G$^-$ and G$^+$-T barriers obtained by Durig et al. through modelling of observed torsional transitions are 1753 and 1005 cm^{-1}, respectively.[34]

Fig. 9(b) compares $\Delta F_{qm;b}(\phi_1)$ for 2FE-$h5$, 2FE-$d1$ and 2FE-$d5$ obtained at both temperatures. At 300 K, all FEPs are essentially the same, as also seen in Fig. 8(b) for the centroid-based FEPs. Interestingly, the 50 K FEPs are also the very similar. In most regions away from the global minimum, $\Delta F_{qm;b}$ is slightly higher with more deuteration.

In order better understand these observations, we have analysed the trends of the mean radii of gyration $\mathcal{R}_g$ of all the atoms of 2FE as a function of ϕ_1. Plots for various atoms at both temperatures and for various H/D isotopomers are shown in Figs. 10, S-5 and S-6. At 300 K, all atoms have practically invariant $\mathcal{R}_g$ values as a function of ϕ_1. This corroborates the similarity of all quantum FEPs at this temperature. However, at 50 K, there are salient $\mathcal{R}_g$ trends. That of the H atom (H_9) of the OH group increases to a fractional extent of 10-15% when ϕ_1 moves away from the global minimum. However, we note that all other atoms also show significant trends. The $\mathcal{R}_g$'s of CH hydrogens, carbons, and the oxygen atoms all increase to a significant fractional extent near $\phi_1 = 0^\circ$. For example, $\mathcal{R}_g(C_1)$ increases by $\sim$20%, $\mathcal{R}_g(H_5)$ increases by about 35% and other CH hydrogens show a similar increase. This suggests that the strong reduction of $F_{qm;b}$ compared to the ab initio barrier may be attributed to a combined effect of which the hydroxyl H is only a part. Note also there is a small but notable increase in the $\mathcal{R}_g$ around the G^+-T barrier region for all atoms, except the hydroxyl H atom whose $\mathcal{R}_g$ increases roughly linearly in this region. Correspondingly, the NQE in this region is small; though the barrier positions and shapes are a little shifted between 50 K and 300 K FEPs, their heights are very similar.

We also note a particular trend for the radii of gyration of the C atoms with isotopic substitution in 2FE. There is an overall lowering of the $\mathcal{R}_g$ at all ϕ_1 values for 2FE-$d5$ compared to 2FE-$h5$ and 2FE-$d1$. That is, the deuteration of all the CH hydrogens reduces the spatial spread of the beads of the C atom as well. There is also a reduction in the $\mathcal{R}_g$ of the OH oxygen with successive deuteration steps albeit to a lesser extent. Note, however, that these changes at 50 K due to H/D substitutions are only incrementally different from the changes in the radii of gyration magnitudes between 50 K and 300 K. The small differences between the $\Delta F_{qm;b}$ for 2FE-$h5$, 2FE-$d1$ and 2FE-$d5$ at 50 K, seen in Fig. 9, may be understood in this light.

The FEPs and atom $\mathcal{R}_g$'s along ϕ_1 discussed above are key results of this work on the NQEs in 2FE in its dihedral space. At ambient temperatures, the NQEs are minor at all ϕ_1 values as evidenced by the small differences between classical and quantum FEPs and the practical invariance of the radii of gyration of all atoms. At low temperature, the NQEs are notable through the same measures, especially as $\phi_1 \to 0^\circ$. As mentioned in the Introduction, Rosenberg has shown,[36] through non-covalent interaction (NCI) analyses and plots along ϕ_1, that the intramolecular OH and F inteaction increases as ϕ_1 decreases from the minimum towards zero (including the appearance of a bond-critical point at $\phi_1 \sim 20^\circ$). The low temperature NQEs trends observed in the present work appear to follow this trail of increasing intramolecular interaction strength as ϕ_1 decreases. However, as ϕ_1 is a large-amplitude low-frequency motion and susceptible to temperature effects, the NQEs in the dihedral landscape are effectively washed out at higher temperatures. We also note that the NQEs on ϕ_2 are effectively a function of ϕ_1; the free energy landscape and hence distribution of ϕ_2 is a function of both temperature and value of ϕ_1, as seen from Fig. S-4.

We briefly return to the markers of the OH and F interaction, viz. the OH bond length, OF and HF distance, and the OHF angle. The average values of these internals as a function of ϕ_1° are shown in Fig. 11. The trends of standard deviations of the distributions are plotted in Fig. S-7. For the analyses, only $-120^\circ \leq \phi_2 \leq 0^\circ$ points are selected when $\phi_1 > 30^\circ$ while points with $-60^\circ \leq \phi_2 \leq 60^\circ$ are chosen when $\phi_1 < 30^\circ$; see Fig. S-4 for the 2D (ϕ_1, ϕ_2) distribution that justifies this choice. Over the wide range of the FCCO dihedral, $\bar{r}_{\mathrm{OH}}$ is effectively invariant. In particular, the values of this internal are nearly the same for the G^+g^- and Cc structures. As seen also in Sec. III C, beyond the zero-point effects, the OH bond length does not provide a marker of the change of interaction between OH and F as a function of the FCCO dihedral. However, the r_{OF}, r_{HF} and θ_{OHF} change significantly. The OH and OF distances are much shorter near $\phi_1 = 0°$ and the OHF angle increases substantially as well as ϕ_1 decreases. However, the effect is largely classical; the results from the PI-US simulations are very similar to it. The NQEs are thus small along the whole umbrella sampling path, not just at the G^+g^- minimum that was discussed in Sec. III C.

F. T-RPMD simulations: Infrared spectra

Fig. 12 shows the spectra of 2FE obtained from T-RPMD simulations at 50 K and 300 K. The spectrum from classical simulations at 300 K is also plotted. The vertical lines indicate experimental band centers taken from Durig et al.[34] The band centers from the present quantum simulations and experiments are compared in Table VIII. The close match indicates the quality of the PES built in this work. The band assignments in Table VIII are based on the normal mode motions visualized at the MP2/aVTZ level and with the assumption that the modes are anharmonically shifted without change of order. Where differently assigned from Durig et al., they are indicated with a $^{\#}$ mark. It must be noted that several modes are mixed and the assignments are indicative of the salient motions.

The FCCO (ϕ_1) and OH (ϕ_2) torsions agree well with the assignment by Durig et al.[34] However, the 308 cm^{-1} and 516 cm^{-1} bands are better assigned to relative motions of CH_2OH and CH_2F units of the molecule; the earlier assignment was to CCF and CCO bends, respectively, but these angular motions are part of both normal modes computed in the present work (symmetric and asymmetric combinations in the low and high frequency bands, respectively). Bands in the mid-IR region are differently assigned in the present work. For instance, the 1208, 1252 and 1351 cm^{-1} band assignments are reordered. Also, the 1088 cm^{-1} band is assigned to an an admixture of the CC extension with CO and CF compression compared to the previous 888 cm^{-1} assignment for this mode. (A still earlier assignment of a combination of CO and CF str is closer to the present result.[29,41]) These assignment differences with Durig et al. may be due to the different levels of theory used (RHF/6-31G** in their work) and choice of scaling of force constants; the latter significantly shifts certain modes to lower frequencies. The experimental band at 1113 cm^{-1} is not directly visible but may be part of the broad high frequency tail of the computed 1100 cm^{-1} band. The descriptions of the bands for the CH_2 wag motions are refined to symmetric and asymmetric combinations, while the scissor motions at slightly higher frequency appear localized at the harmonic level. All four CH stretches (~ 3000 cm^{-1}) in the computed spectrum appear as part of a broad band (~ 150 cm^{-1} FWHM). The OH stretch band is also broad.

In addition to the listed bands, we note low intensity features visible only in the 300 K spectra, viz. small bands around 125 cm^{-1}, 200 cm^{-1} and around 470 cm^{-1}. These are assigned to the FCCO torsion, CCOH torsion, and relative CH_2OH-CH_2F motion for the Tt conformer based on the corresponding harmonic frequencies (see Table S-2). These assignments also corroborate the findings from the Raman spectra by Durig et al. A weak feature at 275 cm^{-1} may also correspond to the Tt conformer (equivalent of the 308 cm^{-1} band for G^+g^-). The presence of these bands only in the 300 K spectra, both quantum and classical, are indicative of differences in initial configurations as well as dynamics at

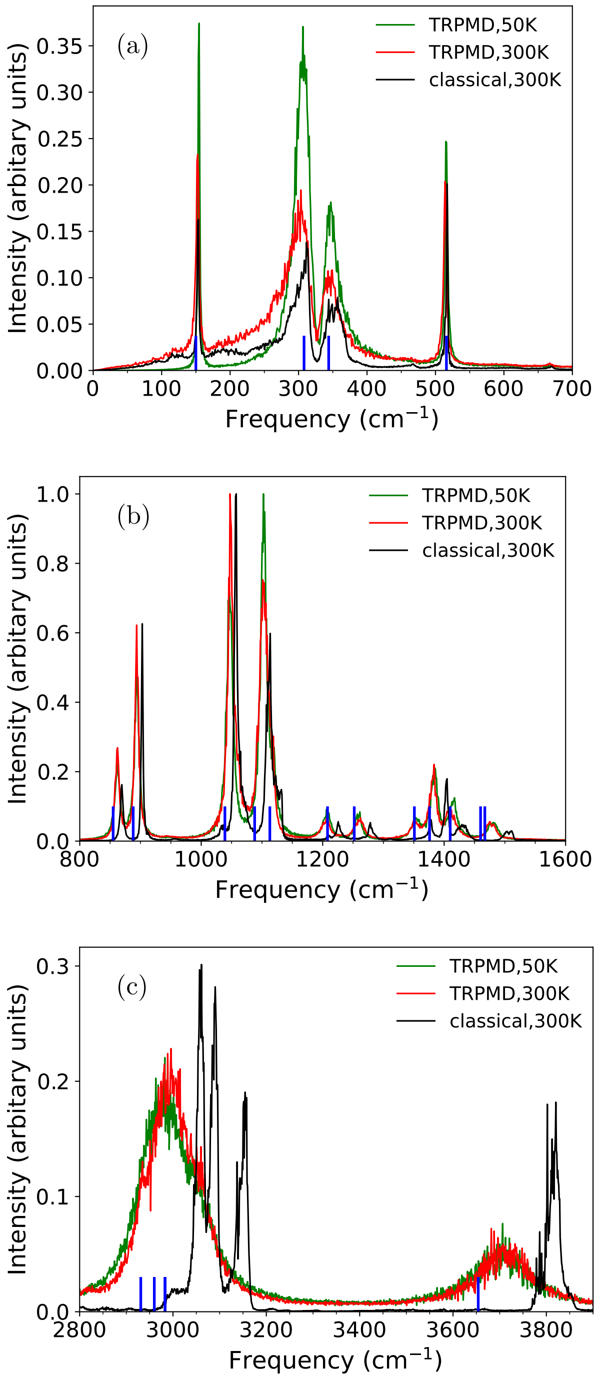

FIG. 12. Infrared spectra at 50 K and 300 K computed with T-RPMD simulations. The classical simulation spectrum at 300 K is also shown. The vertical lines indicate the experimental frequencies taken from Durig et al.[34] The spectrum is shown in the three parts over the ranges (a) 0–700 cm^{-1}, (b) 800–1600 cm^{-1}, (c) 2800-3900 cm^{-1}.

this temperature versus that at 50 K. The PIMD trajectories, from which the initial configurations are sampled for T-RPMD, remain in the G^{+}g^{-} region at 50 K. The T-RPMD

TABLE VIII. Comparison of experimental and computed (T-RPMD) 50 K and 300 K spectral band centers. The former are taken from Durig et al.[34] All values are in cm^{-1}. The band assignments are based on the corresponding harmonic modes at the G$^+$g$^-$ minimum from the present work, assuming that the order of frequencies is maintained. Differences with the experimental study are indicated.

Description[a]	T-RPMD[b]		Expt.
	300 K	50 K	
FCCO torsion	153	154	150
CH$_2$OH–CH$_2$F rel [#]	303	303	308
OH torsion	347	347	344
CH$_2$OH–CH$_2$F rel [#]	514	516	516
CH$_2$ rock[#]	862	861	855
*CH$_2$ rock[#]	894	894	888
*CF–CO asym str[#]	1045	1044	1039
CC, CO, *CF str[#]	1101	1102	1088
COH bend[#]	1207	1206	1208
*CH$_2$ twist[#]	1260	1259	1252
CH$_2$ twist[#]	1350	1354	1351
CH$_2$–*CH$_2$ asym wag	1383	1384	1376
CH$_2$–*CH$_2$ sym wag	1408	1415	1410
CH$_2$, *CH$_2$ scissor	1475	1481	1460 1467
CH str (all)	2990	2982	2931 2960 2983
OH str	3730	3710	3654

[a] Following Durig et al.,[34] asterisks are used to denote the carbon attached to fluorine.

[b] The computed spectra (Fig. 12) are not smoothed. Some bands below 1500 cm^{-1} therefore do not have well-defined peaks (up to about ±5 cm^{-1} wide) and a mean value is reported above. Those for CH and OH stretches have still larger uncertainty.

[#] Assignments different from those of Durig et al.[34]

trajectories at 50 K also remain in this region. However, classical and PIMD trajectories at 300 K sample a much wider range of dihedrals, including the G$^+$g$^-$ and Tt regions. (Note that ϕ_2 conformers are accessed from these regions.) The classical 300 K trajectories start in both regions and sometimes traverse across regions during the simulations. While the 300 K T-RPMD trajectories happen to be so initially sampled that all points are in the G region along ϕ_1, several of them do reach and explore the T region as well. These facets of the dynamics are reflected in the computed spectra.

The comparison of the TRPMD and classical spectra with the experimental band centres suggests that the inclusion of NQEs is important to capture the experimental infrared spectrum in 2FE. Note that both TRPMD and classical spectra are computed with the same anharmonic PES. We parenthetically note that conformer population weighted harmonic spectra (with unscaled frequencies) is blue-shifted relative to the classical spectrum, as shown in Fig. S-8. However, the shift of band centres from the between these two spectra is smaller than that between classical and TRPMD spectra, reiterating the role of NQEs.

The present work suggests that TRPMD offers a satisfactory route for the computation of infrared spectra of molecules with large amplitude motions. Another common approach is conformer population-weighted spectra. The spectra for individual conformers may be obtained from scaled harmonic frequencies,[70] vibrational second order perturbation theory,[71] or more accurate methods.[72] It is non-trivial to obtain reliable conformer populations, though harmonic zero-point corrected relative ab initio energies are a good starting point. One method is to optimize the populations to match spectra; a recent work by Koenis et al. employs a genetic algorithm approach for this task.[70] Another route, closer to the present work, is the use of path integral methods to obtain the relative free energies of the conformers at a given temperature, and hence the populations; early work by Miller and Clary used the path integral Monte Carlo method specialized to torsional degrees of freedom[45,73–75] while a recent work by Riera et al. used replica exchange PIMD.[72] If the barriers between conformations are not too large, so they can be traversed in the course of path integral simulations, then TRPMD from a well-sampled set of initial conditions is the ideal choice within the path integral framework.[76] Of course, methods such as VSCF/VCI may offer more accurate predictions.[77]

IV. SUMMARY

In this work, we have investigated the role of nuclear quantum effects (NQEs) on 2-fluoroethanol (2FE). Through the use of path integral simulations, we have particularly tried to address the role of NQEs (1) on the structure of the molecule in its equilibrium geometry, including the markers of the OH and F interaction, (2) in the free energy landscape of the FCCO and CCOH dihedrals, and (3) in the infrared spectra. As the first step towards such simulations and analyses, we have constructed a full dimensional potential energy surface (PES) in the reaction surface Hamiltonian framework, with special emphasis on the FCCO and CCOH dihedrals. We have additionally modelled a dipole moment surface as well. On the model PES, various quantum (path integral) and classical simulations are carried out.

From both PIMD and classical simulations, we find that the molecule is localized in the minimum energy well at low temperatures (50 - 200 K), but explores other minima including the trans FCCO geometry at 300 K. From the trajectory segments that are in the minimum energy basin, we particularly analyse whether NQEs affect interaction between the OH and

F groups via the trends in the OH, HF and OF distances and the OHF angle. The findings suggest a weak favourable interaction promoted by the NQEs.

We have used biased simulation methods to explore how the free energy landscape differs from the PES and as a function of temperature. Well-tempered metadynamics simulations based on bead centroid biasing show a weak quantum effect with slightly smaller barrier at 50 K compared to 300 K. Focusing on the heavy atom and large barrier FCCO dihedral, we have carried out path integral umbrella sampling simulations. With centroid-based biases, weak quantum effects are seen. However, with bead-based biasing, a substantial decrease in the barrier for FCCO at 0° is seen. Using the radii of gyration of the ring polymers of the atoms as a metric, we found that this effect arises due to the combined effect of all atoms, especially the CH hydrogens and carbons. Interestingly, a recent study by Rosenberg[36] also found an increase of interaction, as measured by the NCI values, between the OH and F groups as the FCCO dihedral is decreased towards 0° . Our findings also indicate that quantum effects do change as a function of the FCCO dihedral at low temperatures and that the backbone C and H atoms play an important role in it.

Finally, we have also computed the infrared spectrum from thermostatted ring polymer molecular dynamics simulations using our model dipole surface. Comparison with experiments gave excellent agreement, indicating the quality of the underlying PES. Contrast with the spectrum from classical simulations reveals the importance of including NQEs for a better match with the experimental spectrum.

2FE may be considered as a model small molecule with a few torsional degrees of freedom for detailed investigations of NQEs. Although the intramolecular interactions are generally weak, our analyses suggest that NQEs nonetheless play a role, whose manifestations can be noted in the structure, free energy landscape and spectra. It would be worth investigating other related molecules with conformational flexibility in a similar vein.

SUPPLEMENTARY MATERIAL

A set of additional tables and figures are provided in the Supplementary Material. These include a comparison of relative energies of minima at various levels of theory, harmonic frequencies of various stationary points at the MP2/aug-cc-pVTZ level of theory, errors in the fitted internals, umbrella sampling parameters, PES quality with a quartic potential, trends of key internals from PIMD simulations, distributions of selected internals in the minimum energy basins, 2D (ϕ_1, ϕ_2) distributions from umbrella sampling simulations, radii of gyration of the ring polymers of all atoms as a function of ϕ_1 at 300 K and 50 K from umbrella sampling simulations, widths of the distributions of selected internals sampled in the minimum basins as a function of ϕ_1, and a comparison of harmonic, classical and TRPMD spectra at 300 K. The Fortran 90 code for the PES for 2FE is available as a tar file as well as here: https://github.com/arandharamrinal/2FE.

ACKNOWLEDGEMENTS

MA thanks the University Grants Commission (UGC) of India and the Indian Institute of Science (IISc), Bangalore, for a research fellowship. The authors thank the Supercomputer Education and Research Centre,IISc, Bangalore, for computational facilities and IISc Bangalore for support with facility charges. The authors also thank the Science and Engineering Research Board of India for computational resources obtained though grant number EMR/2017/003881.

AUTHOR DECLARATIONS

Conflict of Interest

The authors have no conflicts to disclose.

Author Contributions

Mrinal Arandhara: Conceptualization (equal); Data Curation (lead); Methodology (lead); Software (lead); Writing - original draft (lead); Writing - review and editing (equal). **Sai G. Ramesh:** Conceptualization (equal); Supervision (lead); Resources (lead); Writing - review and editing (equal).

DATA AVAILABILITY

The data that support the findings in this study are available from the corresponding author upon reasonable request.

REFERENCES

[1] R. Feynman and A. Hibbs, *Quantum Mechanics and Path Integrals* (McGraw-Hill, New york, 1965).

[2] D. Chandler and P. G. Wolynes, "Exploiting the isomorphism between quantum theory and classical statistical mechanics of polyatomic fluids," J. Chem. Phys. **74**, 4078–4095 (1981).

[3] T. E. Markland and M. Ceriotti, "Nuclear quantum effects enter the mainstream," Nat. Rev. Chem. **2**, 109 (2018).

[4] M. E. Tuckerman, *Statistical Mechanics: Theory and Molecular Simulation (Oxford Graduate Texts)* (Oxford University Press, 2010).

[5] A. Witt, S. D. Ivanov, M. Shiga, H. Forbert, and D. Marx, "On the applicability of centroid and ring polymer path integral molecular dynamics for vibrational spectroscopy," J. Chem. Phys. **130**, 194510 (2009).

[6] M. Shiga, "Path Integral Simulations," in *Reference Module in Chemistry, Molecular Sciences and Chemical Engineering* (Elsevier, 2018).

[7] J. Cao and G. A. Voth, "A new perspective on quantum time correlation functions," J. Chem. Phys. **99**, 10070–10073 (1993).

[8] J. Cao and G. A. Voth, "The formulation of quantum statistical mechanics based on the feynman path centroid density. iv. algorithms for centroid molecular dynamics," J. Chem. Phys. **101**, 6168–6183 (1994).

[9] S. Jang and G. A. Voth, "A derivation of centroid molecular dynamics and other approximate time evolution methods for path integral centroid variables," J. Chem. Phys. **111**, 2371–2384 (1999).

[10] I. R. Craig and D. E. Manolopoulos, "Quantum statistics and classical mechanics: Real time correlation functions from ring polymer molecular dynamics," J. Chem. Phys. **121**, 3368–3373 (2004).

[11] B. J. Braams and D. E. Manolopoulos, "On the short-time limit of ring polymer molecular dynamics," J. Chem. Phys. **125**, 124105 (2006).

[12] S. Habershon, D. E. Manolopoulos, T. E. Markland, and T. F. Miller, "Ring-polymer molecular dynamics: Quantum effects in chemical dynamics from classical trajectories in an extended phase space," Annu. Rev. Phys. Chem. **64**, 387–413 (2013).

[13] S. Habershon and D. E. Manolopoulos, "Zero point energy leakage in condensed phase dynamics: An assessment of quantum simulation methods for liquid water," J. Chem. Phys. **131**, 244518 (2009).

[14] S. Habershon, T. E. Markland, and D. E. Manolopoulos, "Competing quantum effects in the dynamics of a flexible water model," J. Chem. Phys. **131**, 024501 (2009).

[15] A. Kaczmarek, M. Shiga, and D. Marx, "Quantum effects on vibrational and electronic spectra of hydrazine studied by on-the-fly ab initio ring polymer molecular dynamics," J. Phys. Chem. A **113**, 1985–1994 (2009).

[16] X.-Z. Li, B. Walker, and A. Michaelides, "Quantum nature of the hydrogen bond," Proc. Natl. Acad. Sci. **108**, 6369–6373 (2011).

[17] S. Sugawara, T. Yoshikawa, T. Takayanagi, and M. Tachikawa, "Theoretical study on mechanisms of structural rearrangement and ionic dissociation in the hcl(h2o)4 cluster with path-integral molecular dynamics simulations," Chem. Phys. Lett. **501**, 238–244 (2011).

[18] T. E. Markland and B. J. Berne, "Unraveling quantum mechanical effects in water using isotopic fractionation," Proc. Natl. Acad. Sci. **109**, 7988–7991 (2012).

[19] Y. Kawashima and M. Tachikawa, "Ab Initio Path Integral Molecular Dynamics Study of the Nuclear Quantum Effect on Out-of-Plane Ring Deformation of Hydrogen Maleate Anion," J. Chem. Theory Comput. **10**, 153–163 (2013).

[20] C. Drechsel-Grau and D. Marx, "Quantum simulation of collective proton tunneling in hexagonal ice crystals," Phys. Rev. Lett. **112**, 148302 (2014).

[21] P. E. Videla, P. J. Rossky, and D. Laria, "Communication: Isotopic effects on tunneling motions in the water trimer," J. Chem. Phys. **144**, 061101 (2016).

[22] P. Bajaj, J. O. Richardson, and F. Paesani, "Ion-mediated hydrogen-bond rearrangement through tunnelling in the iodide-dihydrate complex," Nat. Chem. **11**, 367–374 (2019).

[23] E. Méndez and D. Laria, "Nuclear quantum effects on the hydrogen bond donor-acceptor exchange in water-water and water-methanol dimers," J. Chem. Phys. **153**, 054302 (2020).

[24] J. R. Cendagorta, H. Shen, Z. Bačić, and M. E. Tuckerman, "Enhanced Sampling Path Integral Methods Using Neural Network Potential Energy Surfaces with Application to Diffusion in Hydrogen Hydrates," Adv. Theory Simul. **4**, 2000258 (2020).

[25] E. Méndez, P. E. Videla, and D. Laria, "Equilibrium and Dynamical Characteristics of Hydrogen Bond Bifurcations in Water-Water and Water-Ammonia Dimers: A Path Integral Molecular Dynamics Study," J. Phys. Chem. A **126**, 4721–4733 (2022).

[26] H. E. Sauceda, V. Vassilev-Galindo, S. Chmiela, K.-R. Müller, and A. Tkatchenko, "Dynamical strengthening of covalent and non-covalent molecular interactions by nuclear quantum effects at finite temperature," Nat. Commun. **12**, 442 (2021).

[27] T. Udagawa, K. Kuwahata, and M. Tachikawa, "Competitive nuclear quantum effect and H/D isotope effect on torsional motion of H2O2: An ab initio path integral molecular dynamics study," Comput. Theor. Chem. **1208**, 113542 (2022).

[28] K. S. Buckton and R. G. Azrak, "Microwave spectrum and intramolecular hydrogen bonding in 2-fluoroethanol," J. Chem. Phys. **52**, 5652–5655 (1970).

[29] M. Perttilä, J. Murto, A. Kivinen, and K. Turunen, "Fluoroalcohols—XXV. matrix i.r. spectrum and normal coordinate analysis of 2-fluoroethanol," Spectrochim. Acta A: Mol. Spectr. **34**, 9–13 (1978).

[30] J. Huang and K. Hedberg, "Conformational analysis. 13. 2-fluoroethanol. an investigation of the molecular structure and conformational composition at 20, 156, and 240 degree. estimate of the anti-gauche energy difference," J. Am. Chem. Soc. **111**, 6909–6913 (1989).

[31] D. A. Dixon and B. E. Smart, "Conformational energies of 2-fluoroethanol and 2-fluoroacetaldehyde enol: strength of the internal hydrogen bond," J. Phys. Chem. **95**, 1609–1612 (1991).

[32] G. Buemi, "Molecular conformations and rotation barriers of 2-halogenoethanethiols and 2-halogenoethanols: an ab initio study," J. Chem. Soc., Faraday Trans. **90**, 1211 (1994).

[33] J. M. Bakke, L. H. Bjerkeseth, T. E. Rønnow, and K. Steinsvoll, "The conformation of 2-fluoroethanol: is intramolecular hydrogen bonding important?" J. Mol. Struct. **321**, 205–214 (1994).

[34] J. R. Durig, P. Klaeboe, G. A. Guirgis, L. Wang, and J. Liu, "Far Infrared Spectra, Conformational Equilibrium, Barriers to Internal Rotation, Vibrational Assignment and ab initio Calculations of 2-Fluoroethanol," Z. Phys. Chem. **191**, 23–45 (1995).

[35] M. Baranac-Stojanović, J. Aleksić, and M. Stojanović, "Energy decomposition analysis of gauche preference in 2-haloethanol, 2-haloethylamine (halogen = F, Cl), their protonated forms and anti preference in 1-chloro-2-fluoroethane," RSC Adv. **5**, 22980–22995 (2015).

[36] R. E. Rosenberg, "Can 2-x-ethanols form intramolecular hydrogen bonds?" J. Phys. Chem. A **123**, 7651–7660 (2019).

[37] N. Sokolov, M. Vener, and V. Savel'ev, "Tentative study of the strong hydrogen bond dynamics," J. Mol. Struct. **177**, 93–110 (1988).

[38] R. H. McKenzie, "A diabatic state model for donor-hydrogen vibrational frequency shifts in hydrogen bonded complexes," Chem. Phys. Lett. **535**, 196–200 (2012).

[39] R. H. McKenzie, C. Bekker, B. Athokpam, and S. G. Ramesh, "Effect of quantum nuclear motion on hydrogen bonding," J. Chem. Phys. **140** (2014), 10.1063/1.4873352.

[40] C. L. Brummel, S. W. Mork, and L. A. Philips, "High-resolution infrared spectroscopy of 2-fluoroethanol in a molecular beam," J. Chem. Phys. **95**, 7041–7053 (1991).

[41] C. C. Miller, L. A. Philips, A. M. Andrews, G. T. Fraser, B. H. Pate, and R. D. Suenram, "Rotational spectrum of a dark state in 2-fluoroethanol using microwave/radio-frequency-infrared multiple resonance," J. Chem. Phys. **100**, 831–839 (1994).

[42] E. Hudspeth, D. A. McWhorter, and B. H. Pate, “Structurally mixed molecular eigenstates of 2-fluoroethanol resulting from conformational isomerization,” J. Chem. Phys. **107**, 8189–8192 (1997).

[43] D. Green, S. Hammond, J. Keske, and B. H. Pate, “Intramolecular vibrational energy redistribution and conformational isomerization in vibrationally excited 2-fluoroethanol: High-resolution, microwave-infrared double-resonance spectroscopy investigation of the asymmetric $-CH_2(F)$ stretch near 2980 cm^{-1},” J. Chem. Phys. **110**, 1979–1989 (1999).

[44] D. A. McWhorter, E. Hudspeth, and B. H. Pate, “The rotational spectra of single molecular eigenstates of 2-fluoroethanol: Measurement of the conformational isomerization rate at 2980 cm^{-1},” J. Chem. Phys. **110**, 2000–2009 (1999).

[45] T. F. Miller and D. C. Clary, “Quantum free energies of the conformers of glycine on an ab initio potential energy,” Phys. Chem. Chem. Phys. **6**, 2563 (2004).

[46] T. E. Markland, S. Habershon, and D. E. Manolopoulos, “Quantum diffusion of hydrogen and muonium atoms in liquid water and hexagonal ice,” J. Chem. Phys. **128**, 194506 (2008).

[47] M. Arandhara and S. G. Ramesh, “Nuclear Quantum Effects in Gas-Phase Ethylene Glycol,” (manuscript in preparation).

[48] M. J. Frisch, G. W. Trucks, H. B. Schlegel, G. E. Scuseria, M. A. Robb, J. R. Cheeseman, G. Scalmani, V. Barone, G. A. Petersson, H. Nakatsuji, X. Li, M. Caricato, A. V. Marenich, J. Bloino, B. G. Janesko, R. Gomperts, B. Mennucci, H. P. Hratchian, J. V. Ortiz, A. F. Izmaylov, J. L. Sonnenberg, D. Williams-Young, F. Ding, F. Lipparini, F. Egidi, J. Goings, B. Peng, A. Petrone, T. Henderson, D. Ranasinghe, V. G. Zakrzewski, J. Gao, N. Rega, G. Zheng, W. Liang, M. Hada, M. Ehara, K. Toyota, R. Fukuda, J. Hasegawa, M. Ishida, T. Nakajima, Y. Honda, O. Kitao, H. Nakai, T. Vreven, K. Throssell, J. A. Montgomery, Jr., J. E. Peralta, F. Ogliaro, M. J. Bearpark, J. J. Heyd, E. N. Brothers, K. N. Kudin, V. N. Staroverov, T. A. Keith, R. Kobayashi, J. Normand, K. Raghavachari, A. P. Rendell, J. C. Burant, S. S. Iyengar, J. Tomasi, M. Cossi, J. M. Millam, M. Klene, C. Adamo, R. Cammi, J. W. Ochterski, R. L. Martin, K. Morokuma, O. Farkas, J. B. Foresman, and D. J. Fox, “Gaussian 16 Revision C.01,” (2016), Gaussian Inc. Wallingford CT.

[49] T. Carrington and W. H. Miller, “Reaction surface description of intramolecular hydrogen atom transfer in malonaldehyde,” J. Chem. Phys. **84**, 4364–4370 (1986).

[50] J. Koput, S. Carter, and N. C. Handy, “Potential energy surface and vibrational-rotational energy levels of hydrogen peroxide,” J. Phys. Chem. A **102**, 6325–6330 (1998).

[51] E. L. Sibert and J. Castillo-Chará, “Theoretical studies of the potential surface and vibrational spectroscopy of CH_3OH and its deuterated analogs,” J. Chem. Phys. **122**, 194306 (2005).

[52] D. P. Tew, N. C. Handy, and S. Carter, “A reaction surface Hamiltonian study of malonaldehyde,” J. Chem. Phys. **125**, 084313 (2006).

[53] Y. G. Smeyers, “Introduction to Group Theory for Non-Rigid Molecules,” Adv. Quantum Chem. **24**, 1–77 (1992).

[54] X. Huang, B. J. Braams, and J. M. Bowman, “Ab initio potential energy and dipole moment surfaces for $H_5O_2^+$,” J. Chem. Phys. **122**, 044308 (2005).

[55] C. R. Harris, K. J. Millman, S. J. van der Walt, R. Gommers, P. Virtanen, D. Cournapeau, E. Wieser, J. Taylor, S. Berg, N. J. Smith, R. Kern, M. Picus, S. Hoyer, M. H. van Kerkwijk, M. Brett, A. Haldane, J. F. del Río, M. Wiebe, P. Peterson, P. Gérard-Marchant, K. Sheppard, T. Reddy, W. Weckesser, H. Abbasi, C. Gohlke, and T. E. Oliphant, “Array programming with NumPy,” Nature **585**, 357–362 (2020).

[56]M. Rossi, M. Ceriotti, and D. E. Manolopoulos, "How to remove the spurious resonances from ring polymer molecular dynamics," J. Chem. Phys. **140**, 234116 (2014).

[57]J. Kästner, "Umbrella sampling," WIREs Comput Mol Sci **1**, 9320942 (2011).

[58]A. Barducci, G. Bussi, and M. Parrinello, "Well-Tempered Metadynamics: A Smoothly Converging and Tunable Free-Energy Method," Phys. Rev. Lett. **100**, 020603 (2008).

[59]A. Barducci, M. Bonomi, and M. Parrinello, "Metadynamics," WIREs Comput. Mol. Sci. **1**, 826–843 (2011).

[60]J. F. Dama, M. Parrinello, and G. A. Voth, "Well-tempered metadynamics converges asymptotically," Phys. Rev. Lett. **112**, 240602 (2014).

[61]O. Valsson, P. Tiwary, and M. Parrinello, "Enhancing important fluctuations: Rare events and metadynamics from a conceptual viewpoint," Annu. Rev. Phys. Chem. **67**, 159–184 (2016).

[62]The PLUMED Consortium, "Promoting transparency and reproducibility in enhanced molecular simulations," Nat. Methods **16**, 670–673 (2019).

[63]A. Grossfield, "WHAM: The weighted histogram analysis method, version 2.0.11," .

[64]A. Lamaire, J. Wieme, S. M. J. Rogge, M. Waroquier, and V. Van Speybroeck, "On the importance of anharmonicities and nuclear quantum effects in modelling the structural properties and thermal expansion of mof-5," J. Chem. Phys. **150**, 094503 (2019).

[65]G. A. Tribello, M. Bonomi, D. Branduardi, C. Camilloni, and G. Bussi, "PLUMED 2: New feathers for an old bird," Comput. Phys. Commun. **185**, 604–613 (2014).

[66]R. Korol, N. Bou-Rabee, and T. F. Miller, "Cayley modification for strongly stable path-integral and ring-polymer molecular dynamics," J. Chem. Phys. **151**, 124103 (2019).

[67]R. Korol, J. L. Rosa-Raíces, N. Bou-Rabee, and T. F. Miller, "Dimension-free path-integral molecular dynamics without preconditioning," J. Chem. Phys. **152**, 104102 (2020).

[68]S. E. Brown, "From ab initio data to high-dimensional potential energy surfaces: A critical overview and assessment of the development of permutationally invariant polynomial potential energy surfaces for single molecules," J. Chem. Phys. **151**, 194111 (2019).

[69]S. Chmiela, H. E. Sauceda, K.-R. Müller, and A. Tkatchenko, "Towards exact molecular dynamics simulations with machine-learned force fields," Nat. Commun. **9**, 3887 (2018).

[70]M. A. J. Koenis, Y. Xia, S. R. Domingos, L. Visscher, W. J. Buma, and V. P. Nicu, "Taming conformational heterogeneity in and with vibrational circular dichroism spectroscopy," Chem. Sci. **10**, 7680–7689 (2019).

[71]P. Das, P. K. Das, and E. Arunan, "Conformational stability and intramolecular hydrogen bonding in 1,2-ethanediol and 1,4-butanediol," J. Phys. Chem. A **119**, 3710–3720 (2015).

[72]M. Riera, J. J. Talbot, R. P. Steele, and F. Paesani, "Infrared signatures of isomer selectivity and symmetry breaking in the $Cs^+ \cdot (H_2O)_3$ complex using many-body potential energy functions," J. Chem. Phys. **153** (2020), 10.1063/5.0013101.

[73]T. F. Miller and D. C. Clary, "Torsional path integral Monte Carlo method for the quantum simulation of large molecules," J. Chem. Phys. **116**, 8262–8269 (2002).

[74]T. F. Miller and D. C. Clary, "Torsional path integral Monte Carlo method for calculating the absolute quantum free energy of large molecules," J. Chem. Phys. **119**, 68–76 (2003).

[75]T. F. Miller and D. C. Clary, "Torsional anharmonicity in the conformational thermodynamics of flexible molecules," Mol. Phys. **103**, 1573–1578 (2005).

[76]S. C. Althorpe, "Path-integral approximations to quantum dynamics," Eur. Phys. J. B **94** (2021), 10.1140/ep jb/s10051-021-00155-2.

[77]Q. Yu and J. M. Bowman, "Classical, Thermostated Ring Polymer, and Quantum VSCF/VCI Calculations of IR Spectra of $H_7O_3^+$ and $H_9O_4^+$ (Eigen) and Comparison with

Experiment," J. Phys. Chem. A **123**, 1399–1409 (2019).